4.3
Turbine Blade Aerodynamics

Sumanta Acharya

Gazi Mahmood

Louisiana State University
CEBA 1419B, Mechanical Engineering Department
Baton Rouge, LA 70803

phone: (225) 578-5809
email: acharya@me.lsu.edu

4.3-1 Introduction

The aerodynamics of the flow in a turbine stage (stator/rotor) is rather complex and is still the subject of many ongoing research activities in the gas turbine community. The flow is inherently three dimensional due to the vane/blade passage geometry with features such as twisting of the vane/blade along the span, clearance between the blade tip and the shroud, film cooling holes, and end wall contouring[1]. The passage flow is characterized by boundary layer effects, secondary flows generated by the passage pressure gradients, and vortical flow structures such as the leading edge horse-shoe vortices, tip-leakage flow vortices, and corner vortices[2]. The effects of centrifugal-buoyancy, shock-boundary layer interaction, and flow interactions between the stator and rotor rows complicate the passage flow field even further. Along the end walls, the flow structure is strongly three-dimensional with the passage vortex and coolant injection on the hub side and the tip-leakage vortex on the tip side. In the mid-span regions located away from the passage walls and outside the viscous shear layer, the radial flow is almost negligible and the flow is effectively two dimensional. The fluid dynamics in this region can then be based on two dimensional planar cascade flow studies without any significant loss of information. The three dimensional complex flow structures near the hub endwall region and in the blade tip-shroud clearance have been simulated in annular vane/blade passages with and without rotating blade row[3]. Studies of the complex end-wall flows have also been performed in stationary cascades with three dimensional airfoil shapes[4]. The qualitative features of the passage flows, which comprise mainly of the passage crossflow (flow from the pressure side of vane/blade to suction side of adjacent vane/blade) and vortical flows induced by the leading edge, the corners, and the injected coolant flows have been studied in detail in stationary cascades and are considered to be similar in both stationary and rotating blade rows. The primary difference in the secondary flow structure between the blade passage and vane passage is that the vortical flows and cross flows in the blade passage are stronger because of higher turning of the flows along the blade passage. Secondary flows are the major source of aerodynamic losses, which account for 35%-40% of all losses[5] and thermal loading in the turbine passage, and thus require special considerations by the turbine designers.

The primary objectives of this chapter are to present and analyze the features of the flow field in the turbine vane/blade passage near the hub endwall and mid-span locations of the blade. Toward this effort, reported measurements and computations of pressure, velocity distributions, flow turning angles, turbulence intensity, and vorticity distributions in the cascade test section are presented. Recent efforts to reduce the secondary flows by structural modifications in the passage are discussed. In this chapter, basic fluid dynamic principles and mathematical models of the flow in the passage are not discussed, and the reader is referred to notes 1, 2, and 6 for additional details[6]. Also details on the aerodynamic design methodology for the vane/blade passage are not presented.

4.3-2 Flow Field in the Mid-span Region

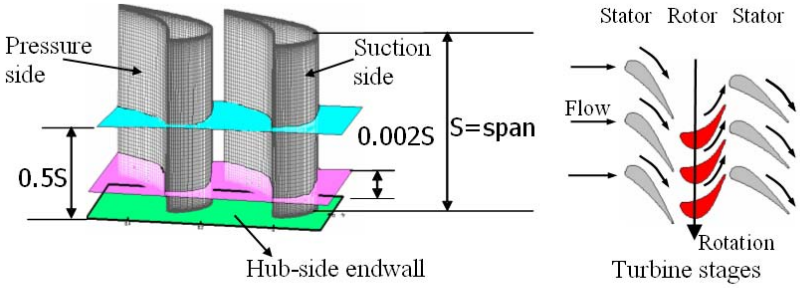

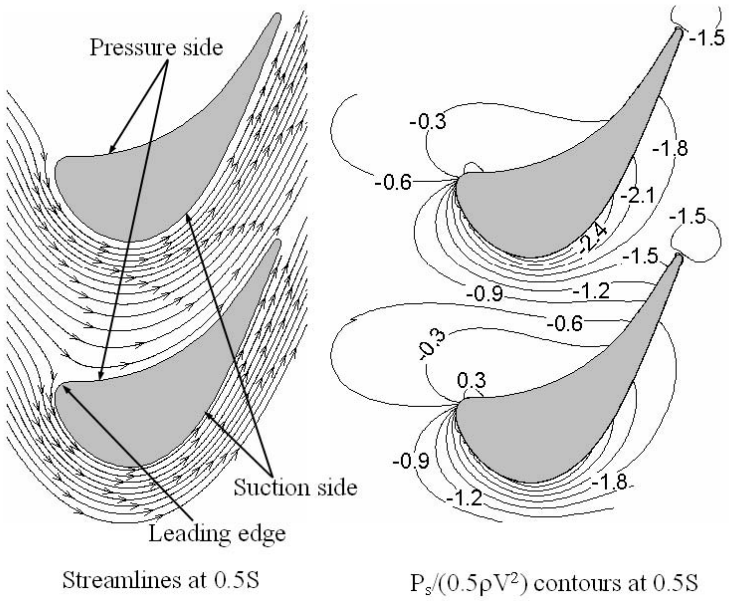

Fig. 1. Streamlines and static pressure distribution in the mid-span plane along blade passage.

Source: See Note 56 (Acharya).

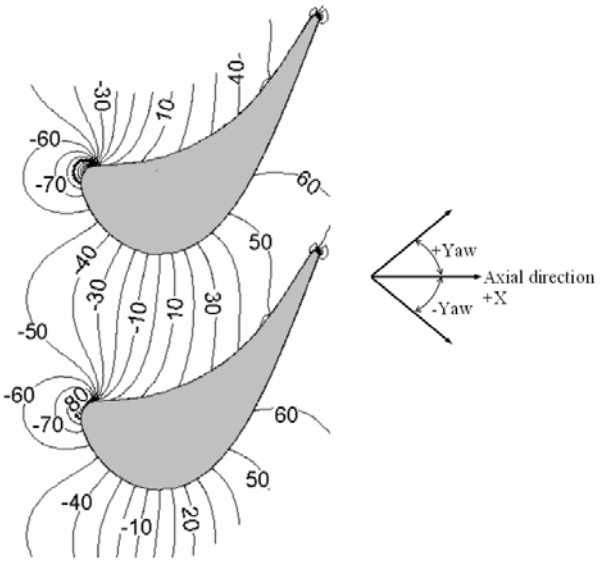

Fig. 2. Flow yaw angle (deg) contours in mid-span plane along blade passage.

Source: See Note 56 (Acharya).

Figure 1 shows the streamlines and static pressure distribution along the mid-span plane of the blade passage. Flow along the blade passage at the mid-span locations turns with the passage contour and essentially follows the ideal flow behavior except very close to the blade walls. At zero degree angle of incidence, the streamline splits at the stagnation point corresponding to the blade leading edge with one leg moving along the pressure side and the other leg moving along the suction side of the blade. The pressure gradient from the pressure side to the suction side leads to the development of secondary flows. These secondary flows and the endwall boundary layer produce deviations to the nearly-inviscid mid-span streamlines shown in figure 2. The flow turning angle, known as the yaw angle relative to the axial +X direction, at the mid-span plane through the blade passage is shown in figure 2. The yaw angle is nearly uniform along a constant pitch line from the pressure side to the suction side, and also changes uniformly along the axial length of the passage. The high yaw angle near the leading edge occurs because of the stagnation region where the streamlines sharply turn around the blade suction side. Figure 3 shows the distribution of the static pressure coefficient, $C_{p,}$ which is determined from the difference of blade surface pressure and reference pressure at the passage inlet normalized by the passage inlet dynamic pressure. The lowest C_p on the suction surface corresponds to the location at the passage throat area where the flow velocity is the highest. The highest C_p is the stagnation point location on the blade section at the mid-span height. The pressure distribution does not change along most of the blade span or height except near the hub or tip region. The blade loading or lift that provides work on the turbine shaft is determined based on the area circumscribed by such pressure curves as shown in figure 3. The pressure side velocity increases steadily as the C_p decreases on the pressure side from the leading edge to the trailing edge. Along the suction surface, the velocity initially increases toward the throat, but starts to decline when it encounters the adverse pressure gradients downstream of the throat in a subsonic flow. The peak velocity in figure 3 corresponds to the location of the minimum C_p on the suction surface.

Due to the adverse pressure gradient on the suction surface downstream of the minimum $C_{p,}$ there is the potential of boundary layer separation from the suction-side blade surface near the trailing edge and this represents a major source of profile losses in the blade passage. Boundary layer separation at the blade trailing edge can also occur due to a finite trailing-edge thickness and can lead to a distinct wake region. For blade profiles with high loading, flow separation is a major issue. With increased loading on the blade surface, suction surface pressures are reduced, and the velocity and Mach number over the suction surface increases with the local Mach number reaching supersonic values. This leads to local shocks as schematically depicted in figure 3, and creates additional aerodynamic losses such as shock losses or wave drag[7]. Downstream of the shock, suction surface pressure rises in the adverse pressure gradient region and

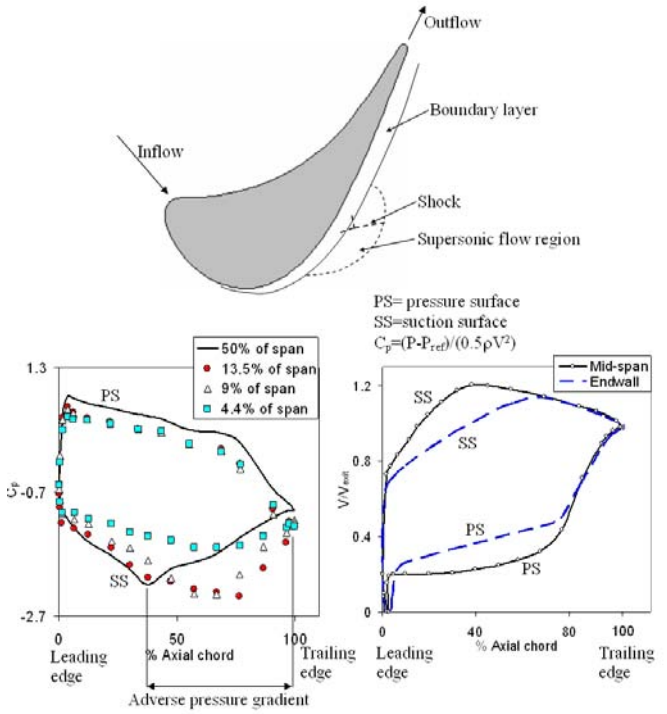

Fig. 3. Pressure and velocity distribution on blade surface at different spanwise locations.

Source: See Note 56 (Acharya).

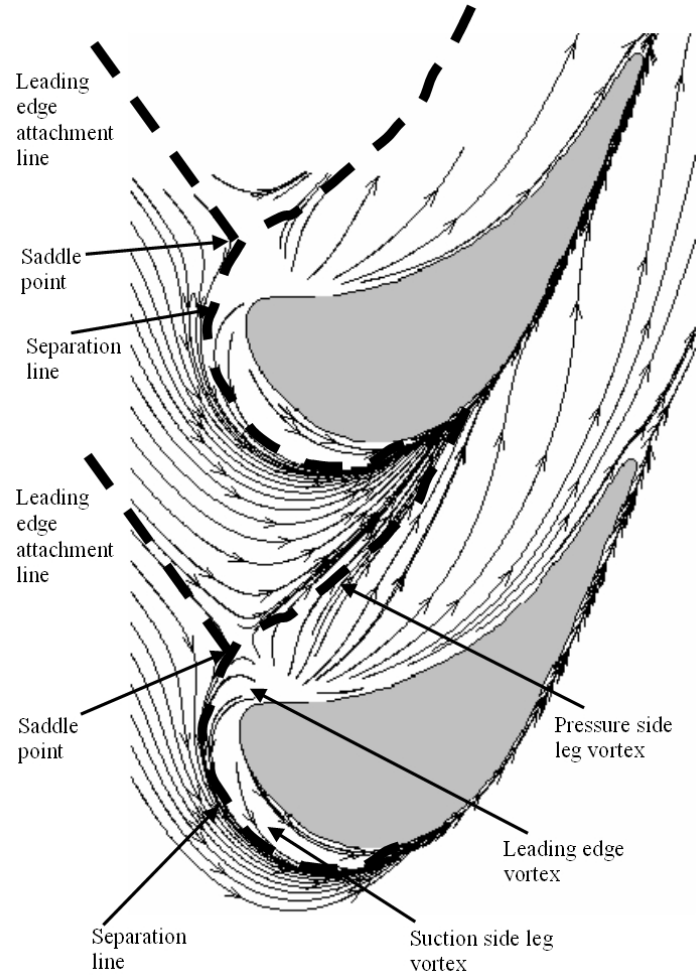

Fig. 4. Streamlines showing separation lines in a near endwall plane of a linear blade passage.

Source: See Note 56 (Acharya).

boundary layer separation can occur earlier leading to increased profile losses for the highly loaded blade. Refer to notes 5 and 8 for discussion on the limiting pressure and velocity distributions on the blade surfaces and provide guidelines to limit the wake region over a very small region at the trailing edge in the blade design[8].

4.3-3 Flow Field in the Endwall Region

The flow field near the hub endwall region of the blade passage is dominated by the boundary layer, strong pressure gradients, and cross flow in the pitchwise direction from the pressure side to the suction side. The resulting near-wall flow field is complex and consists of strong secondary flows and vortex roll-up[9]. When the endwall boundary layer approaches the blade row, a vortex is formed near the junction of the blade leading edge and the endwall. This vortex is termed as the leading edge horse-shoe vortex. The horse-shoe vortex splits at the leading edge, and propagates downstream into the passage on both the pressure side and the suction side of the blade passage forming two legs of the early passage vortex flows. Corner vortices are also induced in the corner formed by the blade and the hub endwall.

The streamlines slightly above the endwall in figure 4 show some distinct features of the endwall boundary layer flow. These features are identified by the separation lines in the figure. The streamlines along the blade leading edge bifurcate as they approach the saddle point. The saddle point is the location on the endwall where the zero degree incidence line meets the separation line and corresponds to the lowest friction velocity. The incoming endwall boundary layer detaches along the separation line, and secondary vortical flows are formed in the regions immediately downstream and adjacent to the separation line. This is indicated by the high concentration of the streamlines adjacent to the separation line. The strong reverse flow in the vortex regions counter the boundary layer streamlines causing them to be concentrated more densely near the separation line. The leading edge horse-shoe vortex immediately downstream of the saddle point is clearly evident in figure 4. The region between the separation line and the blade suction side in figure 4 represents the suction-side leg of the horse shoe vortex[10]. The region along the separation line directed from the pressure side to the suction side represents the pressure-side leg of the horse-shoe vortex[11], and is driven by the passage pressure gradients. The suction side leg vortex and pressure side leg vortex meet together in the mid-passage region where the two separation lines in the passage merge. This location occurs close to the suction surface, and the merger of the two vortices forms a stronger vortex known as the passage vortex. The passage vortex then travels along the blade suction surface toward the passage exit. The axial development and structures of these vortex flows will be analyzed further in Section 4.3-4.

Downstream of the pressure side separation line, the endwall boundary layer region is very thin and skewed toward the suction side. This is evidenced by the streamline concentration being sparse in this region as they turn from the pressure side to the suction side. The strong vortical motions of the pressure side leg vortex entrain most of the fluid from the incoming boundary layer and a new boundary layer forms downstream. Comparing the streamlines in figure 4 with those in the mid-span regions in figure 1, it is clear that the turning of the streamlines inside the blade passage and around the leading edge is much greater near the

endwall region which causes the cross flow here to be stronger. The flow yaw angle contours along the passage in figure 5 show the higher magnitudes of the flow turning near the endwall compared to the flow turning in the mid-span regions away from the endwall.

The endwall pressure gradients are shown in figure 6. The suction side pressure magnitudes along the endwall are higher compared to the suction side pressure values in the free-stream region (see figure 1). This results in smaller pressure gradients in the endwall from the pressure side to the suction side as shown in the line plot of figure 6. The magnitude of ΔP in the figure is the pitchwise pressure difference between two points at the same axial chord location, one located on the pressure side and the other on the suction side. As mentioned earlier, the turning of the boundary layer fluid in the endwall region is much higher compared to the turning of the free-stream in the passage, which seems to contradict the results in figure 6. According to Niehuis, et al., in the free-stream flows away from the endwall, equilibrium exists between the pitchwise pressure gradient and centrifugal force on the fluid elements at the curved streamlines[12]. This equilibrium breaks down in the endwall region because the centrifugal force on the fluid elements in the low velocity boundary layer reduces. As such, the weak endwall region streamlines easily turn to a greater degree with relatively smaller pressure gradients as those in figure 6.

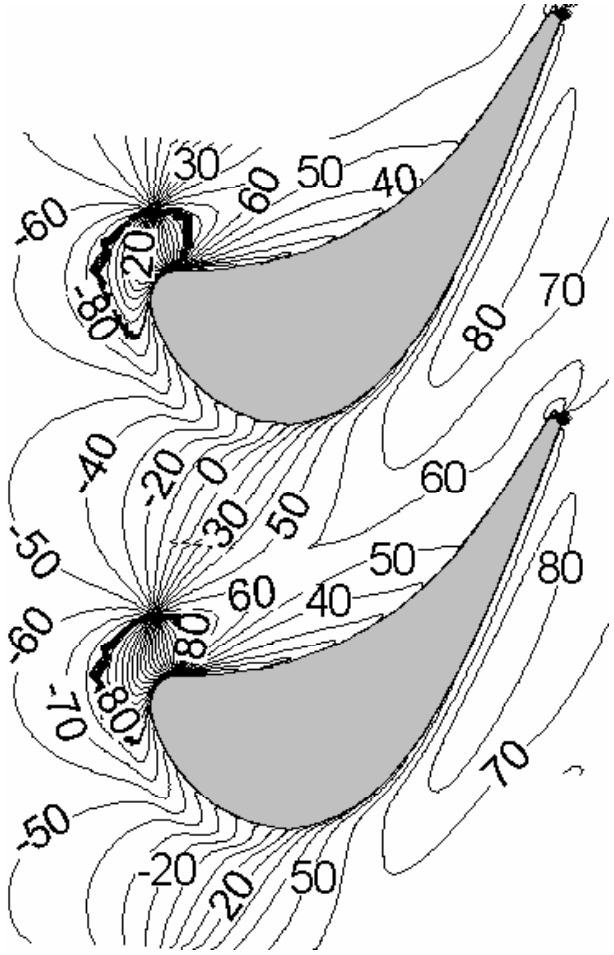

Fig. 5. Flow yaw angle (deg) contours in a plane near endwall along a linear blade passage.

Source: See Note 56 (Acharya).

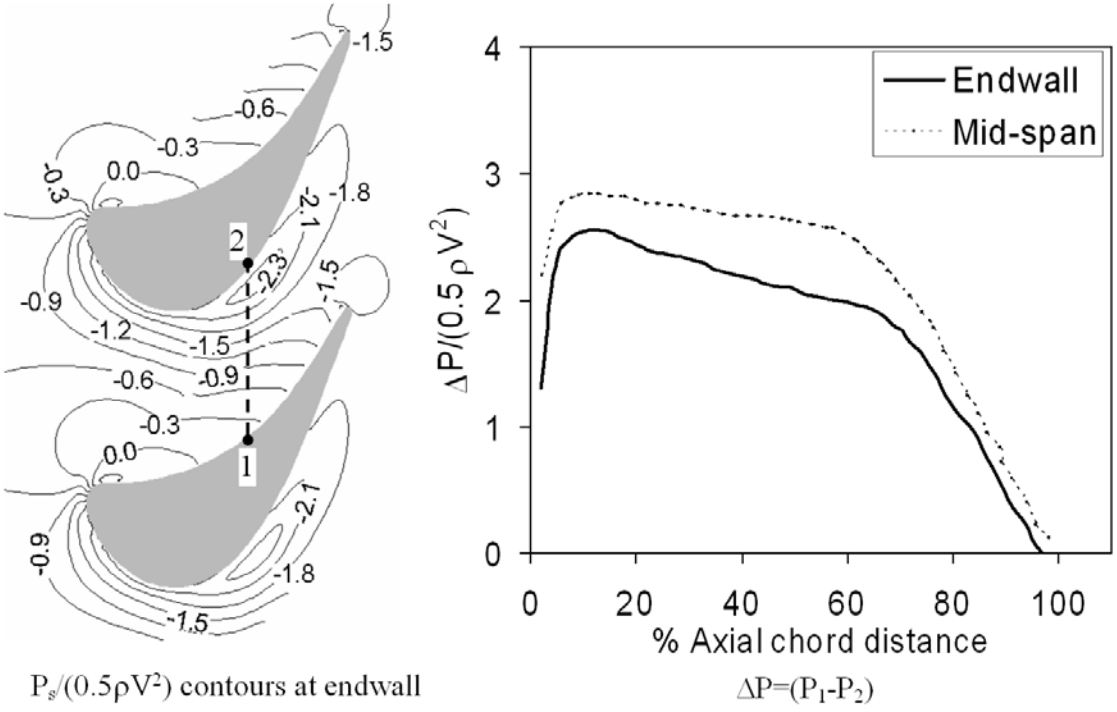

Fig. 6. Surface pressure distribution at endwall of a blade passage in linear cascade.

Source: See Note 56 (Acharya).

The axial pressure distributions along the blade surface (figure 3) change with the span location. The region below 14% span can be considered to be the boundary layer region in the figure. The difference between the free stream static pressure coefficient and endwall region static pressure coefficient C_p on the pressure surface is small and almost uniform. This suggests that pressure gradient on the pressure surface occurs mostly in the axial direction rather than in the spanwise direction. The differences in the suction surface C_p between the 50% span and below 14% span in figure 3 are significant and occur because of the strong cross flow from the pressure side to the suction side in the endwall boundary layer and the vortex leg along the suction surface[13]. The locations of the lowest C_p within the boundary layer occurs further downstream of the lowest C_p location in the mid-span free-stream region. The endwall cross flow drives the low momentum boundary layer fluid toward the suction surface-endwall junction and causes these observed differences in the C_p distributions. This is also the reason why the axial location of the lowest C_p in the boundary layer and the lowest P_s on the endwall are different. Also note that C_p magnitude decreases significantly from the endwall (i.e. 4.4% span) to the boundary layer edge (i.e. 13.5% span) all along the axial direction. Such spanwise pressure gradient drives the boundary layer fluid and the endwall region secondary flows toward the mid-span direction near the suction surface. The implications of such migrations are realized in the Heat Transfer Analysis section.

The velocity distribution on the blade surface near the endwall is also shown in figure 3. The suction surface velocity in the endwall region is lower compared to the free-stream velocity in mid-span because of the influence of strong secondary flows and higher C_p around the suction side edge (i.e. at 4.4% span). As with the lowest C_p location, the associated peak suction surface velocity in the endwall region also moves down the axial direction relative to the peak velocity location at the mid-span. The difference in velocity distribution on the pressures side is opposite to what is observed on the suction surface between the mid-span location and endwall region. This can be attributed to the smaller pressure surface C_p near endwall as well as the thin boundary layer, which is also skewed and thicker toward the suction surface, downstream of the endwall separation line.

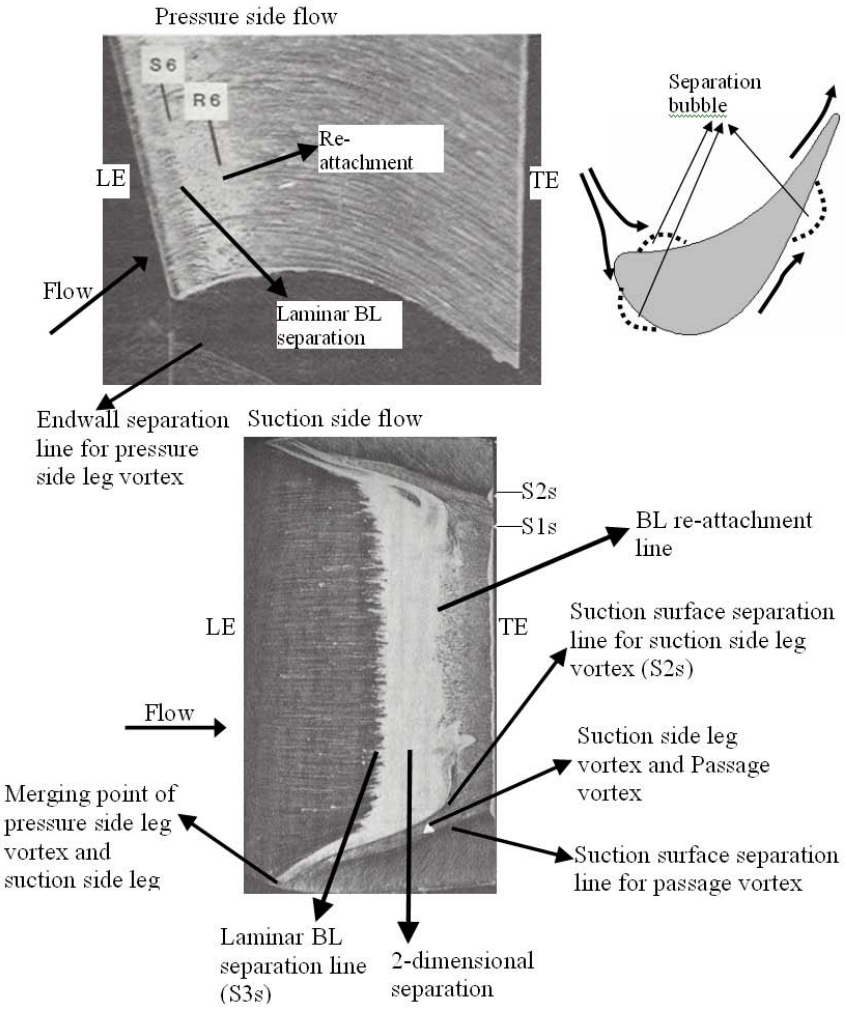

Fig. 7. Surface oil-flow visualization on a linear blade surface and end-wall in a linear cascade. LE= leading edge, TE= trailing edge, and BL= boundry layer

Source: See Note 14.

With the knowledge of velocity and pressure distribution on the blade surface at the mid-span and near endwall, it is now appropriate to discuss the three dimensional flow on the blade surface as a whole. It is apparent by now that the blade suction surface flow near the endwall wall region becomes skewed and three dimensional due to the interaction of the boundary layer and flow separation on the suction surface and endwall. The flow visualization on the suction surface of a two dimensional linear blade in figure 7, as observed in Hodson and Dominy, clearly shows the near surface flow behavior[14]. The flow on the pressure surface is two dimensional for most part of the span as the oil streaklines indicating the surface streamlines are parallel to the endwall in the upper flow visualization of figure 7. The uniform pressure distribution along the pressure surface span (see figure 3) and very weak interaction of the boundary layers between the pressure surface and endwall are responsible for such flow behavior. However, the laminar boundary layer near the pressure surface leading edge may diffuse with a rise in surface pressure when the incoming flow is at high speed. In this case, the boundary layer separates along the line S6 and re-attaches along the line R6 creating a closed separation bubble along most of the span near the leading edge. The laminar boundary layer accelerates following the re-attachment and continues to grow along the pressure surface toward the trailing edge. The two-dimensional separation bubble has no apparent influence on the secondary flows on the endwall.

Near the leading edge at the endwall, the pressure surface streamlines are inclined toward the endwall indicating the flow is driven by the horse-shoe vortex.

The separation lines created by the oil streaklines on the suction surface of figure 7 reveals some interesting features of the boundary layer behavior. The separation lines divide the flow on the suction surface into three regimes: (i) two dimensional laminar boundary layer regime, (ii) turbulent boundary layer regime, and (iii) three dimensional flow regime. (i) *Two dimensional laminar regime*: This regime extends from the leading edge to the lowest suction pressure on the suction surface and between the S2s separation lines near the two endwalls in figure 7. The surface streamlines are seen to be nearly parallel to the endwall in this regime. The laminar boundary layer starting at the leading edge undergoes a high acceleration on the suction surface. According to Hodson and Dominy, the over-acceleration in the boundary layer causes a two dimensional separation bubble near the blend point of the circular leading edge and the suction surface[15]. This separation bubble extends across most of the span, but it is not apparent in the bottom surface flow visualization of figure 7. The suction surface leading edge separation bubble is shown by the flow visualization in Gregory-Smith et al.[16]. Following the re-attachment behind the separation bubble, the laminar boundary layer accelerates along the suction surface and continues to grow until the separation line S3s. (ii) *Turbulent regime*: This regime is limited by the re-attachment line following the separation at S3s and trailing edge and between the S2s lines. The laminar boundary layer separates at the lowest suction pressure located at axial distance at S3s because of the adverse pressure gradient (see figure 3) and forms another closed separation bubble. The boundary layer undergoes transition and becomes turbulent as it re-attaches behind the separation bubble on the suction surface. The turbulent boundary layer grows along the suction surface and may separate again due to the adverse pressure gradient near the trailing edge to form the trailing edge wake. (iii) *Three dimensional flow regime*: This regime is indicated by the region between the separation line S2s and endwall. The regime begins at the location where the suction side leg of the leading edge horse-shoe vortex and pressure side leg vortex from the adjacent blade meet on the suction surface. The pair then emerges as the passage vortex which then moves toward the mid-span as it follows the suction surface toward the passage exit. The suction surface boundary layer separates along the S1s and S2s lines near endwalls in figure 7 as the passage vortex and suction side leg vortex climbs up the suction surface. The distinct appearance of the separation line S2s indicates that the suction side leg vortex maintains its existence in the axial development of the passage vortex which will also be shown in further detail in the next section. The inclination of the surface streamlines toward the mid-span in this regime is caused by the entrainment of the boundary layer fluids (both at the endwall and the suction surface) by the passage vortex. Note that the surface streamlines are symmetric about the mid-span of the blade surface in figure 7. The patterns become asymmetric in three-dimensional cascade by the influence of radial forces as will be shown in further sections.

The locations of the separation bubbles and separation lines on the blade surface are strongly influenced by the inlet flow angle and Reynolds number or Mach number of the incoming flow. For the high speed compressible flow (with the Mach number>0.70), the flow expands and accelerates along the passage creating local supersonic region at the passage throat[17]. As a result, a series of weak compression fans are developed at the suction surface near the throat. Detemple-Laake also shows that at transonic and supersonic flow, shocks are formed across the span at the trailing edge of the blade surface[18]. The shock at the suction surface trailing edge is deflected by the wake from the adjacent blade trailing edge. The shock at the pressure side trailing edge is reflected at the adjacent blade suction surface as a sequence of compression-expansion-compression waves. At all Mach numbers tested (exit Mach number ranges between 0.70 and 1.3), schlieren photographs show that flow separates locally from the blade pressure surface and suction surface forming separation bubbles similar to the subsonic flow pattern[19]. The separation lines for the suction side leg vortex and the passage vortex on the suction surface move nearer to the mid-span as the Mach number is increased. The suction side leg vortex is deflected by the shock from the adjacent blade pressure side trailing edge and moves closer to the passage vortex at supersonic flow. The endwall pressure distributions for high speed compressible flows show the same behavior as that at the low speed flows. Static pressure on the endwall increases slightly at the trailing edge due to the expansion at the trailing edge.

4.3-4 Development and Structure of Secondary Flows in the Passage

We have shown in the earlier section that the secondary flows in the turbine vane/blade passage are dominated by the vortex flows located in the hub endwall region. So far, these vortex flows have been deduced from pressure distributions, near-wall streamlines and saddle points or surface oil-flow visualizations. The vortex flows have been identified as the suction side leg and the pressure side leg originating from the leading edge horse-shoe vortex that eventually merge in a complex way to form the passage vortex. The three vortex structures (horse-shoe, pressure side leg, suction side leg) are the primary sources of the vortex flows in the passage. In addition, smaller corner vortices are induced at the corner of blade edge at the endwall. Vortices are also induced on the suction side near the meeting point of the pressure side leg vortex and suction side leg vortex flows and are advected with these legs along the suction surface toward the passage exit. This section will discuss the structure and development of the three primary vortex flows along the passage at different axial locations by presenting the flow visualization images, streamlines, pressure losses, vorticity, turbulence intensity, and flow turning angles. The induced vortex flows will be identified later in the section.

Leading edge horse-shoe vortex:

The leading edge horse-shoe vortex is formed at the junction of an endwall and the blunt leading edge of the blade. As the flow approaches the leading edge stagnation line, static pressure rises across the flow from the endwall. The static pressure increases more in the free-stream region above the boundary layer since the free-stream velocity is higher compared to the velocity in the boundary layer[20]. This spanwise pressure gradient in the vicinity of the leading edge causes a vortex roll-up, known as the leading edge horse-shoe

vortex. The vortex is confined in a region which is smaller than one boundary layer thickness from the endwall[21]. The endwall location where the reverse flow in the horse-shoe vortex meets the incoming boundary layer flow is termed as the saddle point which is generally located along the line corresponding to the zero degree incidence-angle as shown in figure 4. The center of the horse-shoe vortex is located in between the saddle point and the blade leading edge. The exact locations of the saddle point and horse-shoe vortex center depends on the radius of curvature of the blade leading edge and the oncoming boundary layer thickness. The flow visualization in figure 8 shows the typical formation of an instantaneous horse-shoe vortex at the blade leading edge in a linear cascade[22]. In the figure, the roll-up of the vortex is in the counter-clockwise direction. Periodically, a pair of horse-shoe vortices form that have the same relative size and the same sense of rotation. The time-averaged structure of the horse-shoe vortex obtained from a numerical simulation at the same blade leading edge is also shown in figure 8. The vortex structure is similar to the leading edge horse-shoe vortex in front of a cylinder[23]. The vortex center in figure 8 is located at the point of the maximum kinetic energy. At the corner of the leading edge, a small counter rotating vortex is induced by the large horse-shoe vortex. This clockwise rotating vortex is known as the leading edge corner vortex.

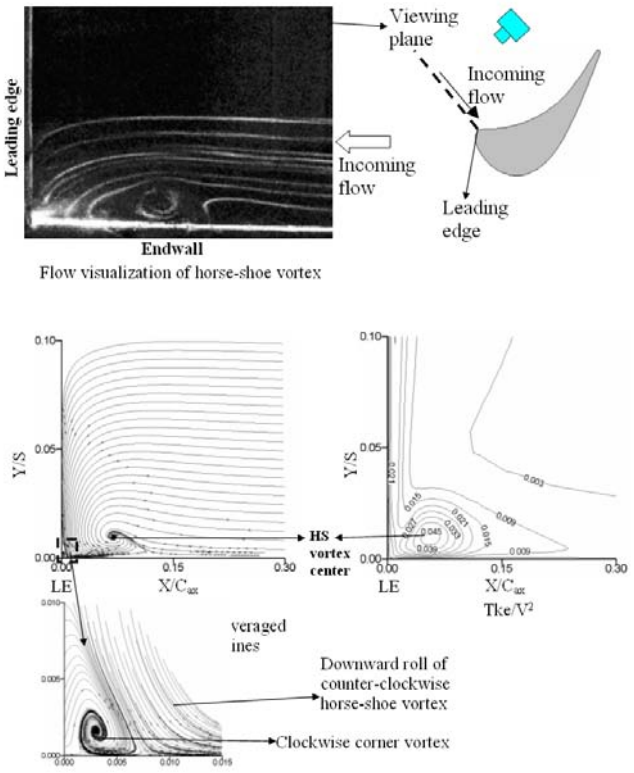

Fig. 8. Typical horse-shoe vortex and corner vortex at a blade leading edge. HS=horse-shoe, LE=leading edge, and Tke=turbulent kinetic energy.

Source: See Notes 22, 56 (Acharya).

Pressure side leg and suction side leg vortices:

The path of the leading edge horse-shoe vortex is along the separation line shown in figure 4, and is driven by the endwall region pressure gradient and cross flow. The horse-shoe vortex essentially splits near the leading edge with one leg moving along the pressure side and the other leg moving along the suction side. These two primary legs of the horse-shoe vortex represent the origin of the major secondary flow system that develops in the blade passage. The two legs rotate opposite to each other. The pressure side leg of the horse-shoe vortex is driven along the separation line across the passage from the leading edge to the adjacent blade suction side. The suction side vortex leg wraps around the suction side from the leading edge along the separation line in figure 4. The vortices are termed as the right side clockwise and left side counter-clockwise vortices, respectively, in the flow visualization images in figure 9[24]. The vortices in the figure are being viewed in the flow direction in pitchwise planes at different axial locations. The pressure side and suction side of the blade passage in the study are located on the right and left hand side, respectively, in the images. At location A, which represents the pitchwise plane going through the leading edge, a pair of vortex structures appears along both the pressure side leg and suction side leg of the vortex system. As with the leading edge horse-shoe vortex pair, these pairs form periodically from a single pressure side and suction side leg vortex. The vortices are very close to the passage pressure side and suction side at plane A. As the vortex legs advect to farther downstream locations at planes B, C, and D in the passage in figure 9, the endwall cross flow and pressure gradient from the pressure side to the suction side sweeps the pressure side leg of the vortex toward the suction side of the passage. As a result, the pressure side vortex approaches closer to the suction side leg vortex from the adjacent blade at the downstream locations. Nearly half way down the passage at location D, the two vortex legs merge to form a single structure

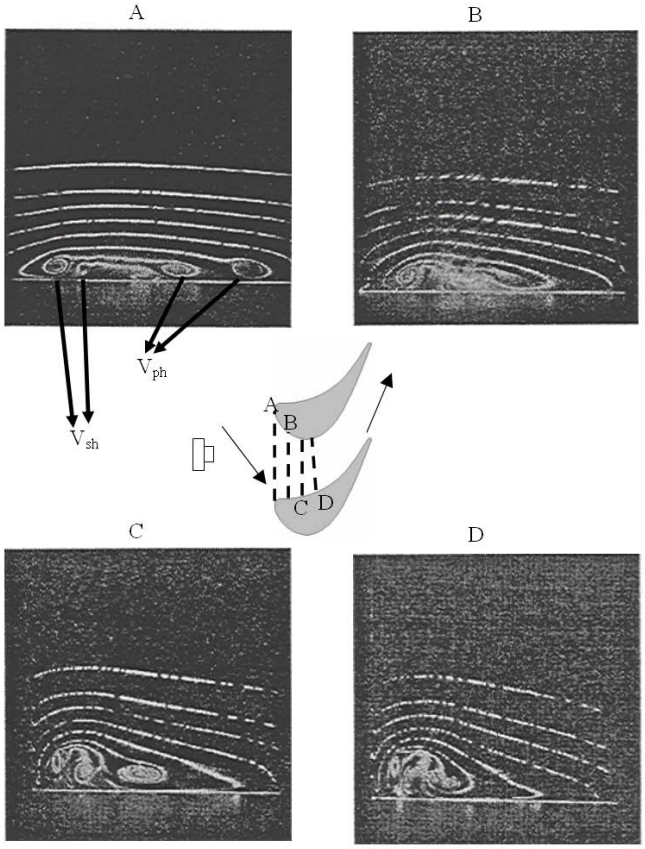

Fig. 9. Flow visualization of pressure side leg and suction side leg vortices from. Vph= pressure side leg vortex and Vsh=suction side leg vortex.

Source: See Note 9.

of counter-rotating vortices. At the merging point, the clockwise pressure side leg vortex is larger and stronger compared to the smaller suction side leg vortex. Note that the vortices remain close to the endwall from the leading edge location to their merger location half way through the passage.

The time-averaged vortex structures, as shown in figure 10, are obtained at a pitchwise plane near the leading edge for a much higher Reynolds number than that used for the flow visualization[25]. Even though the blade geometries are different for the data in figures 9 and 10, the basic structure of the vortices such as the sense of rotation and relative locations are similar. The positive axial vorticity in figure 10 signifies a clockwise rotation of the pressure side leg vortex, while the negative axial vorticity indicates a counter-clockwise rotation of the suction side leg vortex. The small vortex located at the edge of the pressure side and rotating counter-clockwise is termed as the pressure side leading edge corner vortex in Wang, et al. [26]. This vortex is induced by the leading edge horse-shoe vortex and driven along the pressure side leg vortex.

Passage vortex and induced vortices:

The passage vortex is comprised of the pressure side leg vortex and suction side leg vortex as these vortex legs approach and merge with each other nearly half-way into the passage and along the suction side of the blade. This is shown as a counter-rotating vortex pair at location D in Fig. 9. As the pressure side leg vortex is much larger and stronger compared to the suction side leg vortex when they meet, the sense of rotation of the passage is considered be the same as the rotation of the pressure side leg vortex. The passage vortex remain close the suction surface of the blade as it is driven toward the passage exit by the cross flow and pressure gradient along the passage. Figure 11 shows the passage vortex formation in the same passage as in figure. 9 at locations downstream of plane D. The suction side is located on the left hand side in the flow visualization images[27] in figure 11. At locations E and F, the passage vortex V_p is rotating counter-clockwise while the suction side leg vortex V_{sh} is rotating clockwise as they are viewed opposite from the main flow direction. As both the vortices funnel boundary layer fluid and main flow toward their centers, the passage vortex gradually grows larger in size and lifts above the endwall as it travels along the suction surface toward the passage exit. The passage vortex movement toward the mid-span is caused primarily by the spanwise pressure gradient in the boundary layer on the suction surface. Because of this movement of the passage vortex and as the endwall boundary layer fluid is wrapped around the passage vortex, the endwall boundary layer becomes skewed and thicker toward the suction side. The suction side leg vortex wraps around the passage vortex as it travels along with it. This is evidenced in the flow visualization in figure 11. At location E, the suction side leg vortex V_{sh} is located at the top right hand corner of the V_p. At the downstream F location, V_{sh} moves to the left side of the V_p. At the passage exit, a study in Wang, et al. shows that V_{sh} moves around further and is located at the passage vortex bottom part near the suction surface[28].

In the plane F of figure 11, the small clockwise rotating vortex V_{wip} located adjacent to the suction surface and above the passage vortex is termed as the wall vortex. This vortex is formed by the strong induction of the passage vortex and

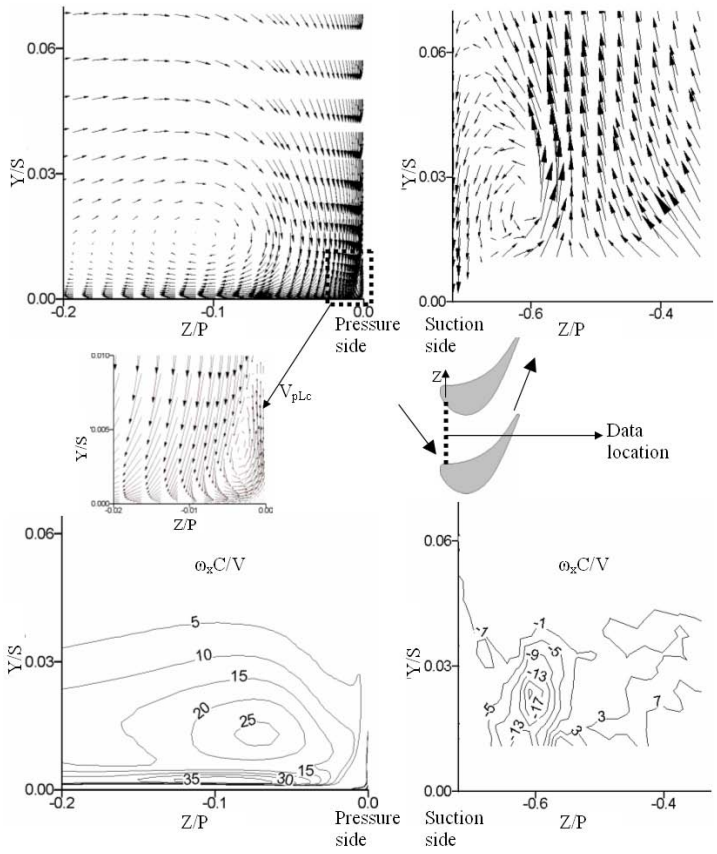

Fig. 10. Velocity vectors and axial vorticity representing pressure side leg vortex and suction side leg vortex near LE. VpLc=pressure side LE corner vortex and ωx=axial vorticity.

Source: See Note 25.

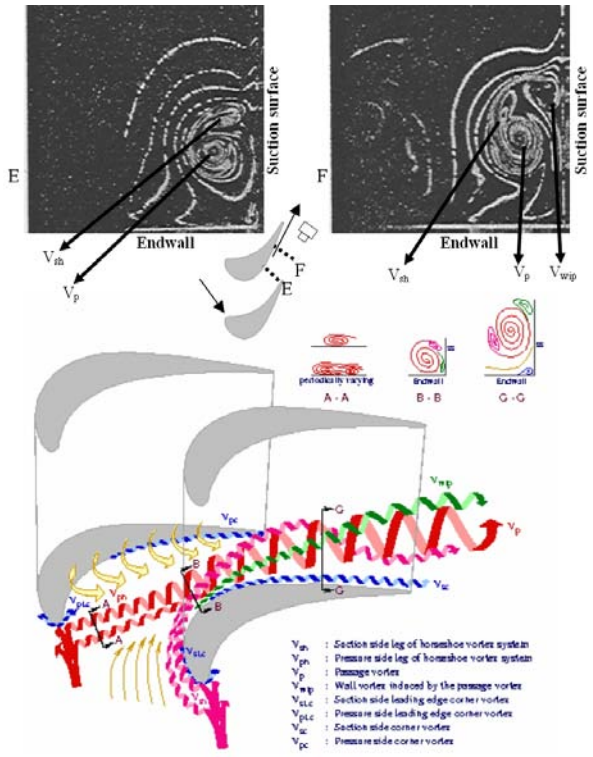

Fig. 11. Flow visualization of passage vortex and induced vortices.

Source: See Note 9.

originates at the same location where the passage vortex starts to form (merging point of the counter-rotating vortex legs). The wall vortex stays above the passage vortex and is driven along with the passage vortex.

The small corner vortex induced at the junction of blade leading edge and endwall (see figure 8) by the horse-shoe vortex is driven along the pressure side and suction side edge with the two main vortex legs. In Wang, et al., they are identified as the pressure side leading edge vortex and suction side leading edge vortex, respectively[29]. They remain small as they travel inside the passage and their sense of rotation are opposite to the rotation of the main vortex legs they are associated with. The pressure side leading edge corner vortex sticks along the pressure surface corner near the leading edge as shown in figure 10. When it enters the passage farther downstream, it is also driven toward the suction side of the adjacent blade along with the pressure side leg vortex by the endwall cross-flow and pressure gradient. The suction side leading edge corner vortex on the other hand remains adjacent to the suction side edge until it meets with pressure side leg vortex from the neighboring blade. The corner vortices are not visible in the smoke flow visualization as the large vortex legs entrain most of the smoke in the flow and enough smoke is not available to generate their small patterns clearly. The three-dimensional structures of different vortex flows in a blade passage sketched in figure 11 are adopted directly from Wang, et al.[30]. The sketch shows two additional small vortex flows located along the pressure surface corner and suction surface corner. They originate about half way downstream in the passage. The existence of such corner vortices is indicated by the high local mass transfer results at the blade surface-endwall corner in Goldstein et al.[31]. These corner vortices rotate in the same direction as the rotation of the suction side leg vortex.

The time-averaged structures of the passage vortex in the same flow as in figure 10 are shown at two axial locations in figure 12. The data presented is measured with a five-hole pressure probe[32]. The velocity vectors are determined based on the resolved components[33]. The plane H in figure 12 is located about half way down the passage and the plane I is located near the exit of the passage. Unlike figure 11, the flow is being viewed in the axial direction and therefore, the suction surface is on the left hand side in the plots of figure 12. Thus, the rotation of the passage vortex is in the clockwise direction in the velocity vector plots. The existence of the suction side leg vortex is not apparent in the vector plots as it becomes weak in the downstream locations. In a small region just above the passage vortex and adjacent to suction surface at plane I, the vectors seem to turn counter-clockwise indicating the presence of the wall vortex or suction side leg vortex. However, the vortex is clearly apparent in the vorticity plots in figure 12. The positive axial vorticity indicates the passage vortex while the negative axial vorticity located above the positive region indicates the suction side leg vortex or the wall vortex. The same arrangement of the vortex systems in the downstream locations have been observed in the flow visualization. The vortex center is located at the location of the maximum vorticity in congruence with the forced vortex motion.

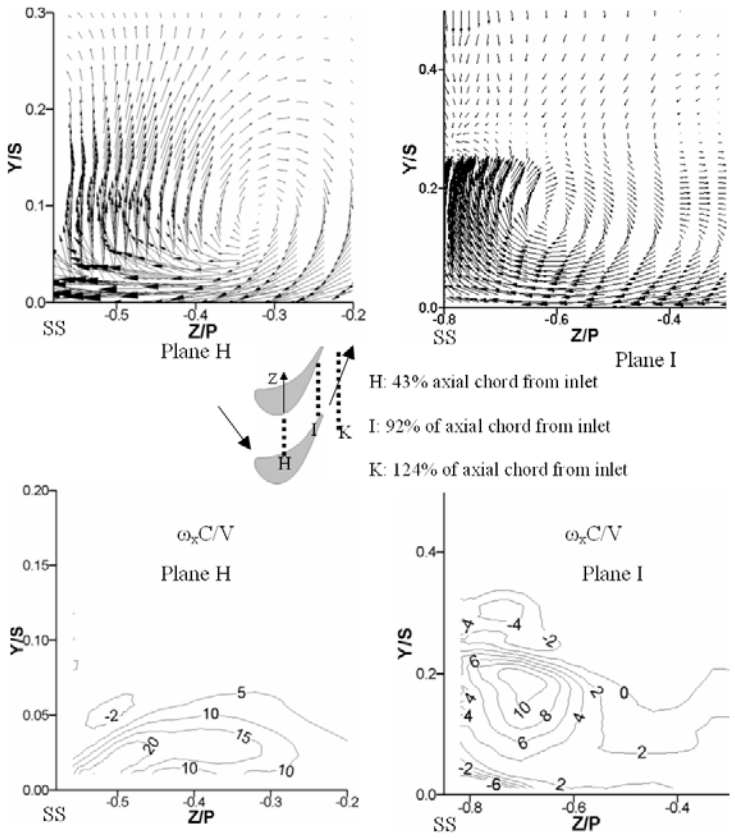

Fig. 12. Velocity vectors and axial vorticity representing passage vortex at suction side. SS=suction side, Z=pitchwise distance from pressure side, and ωx=axial vorticity.

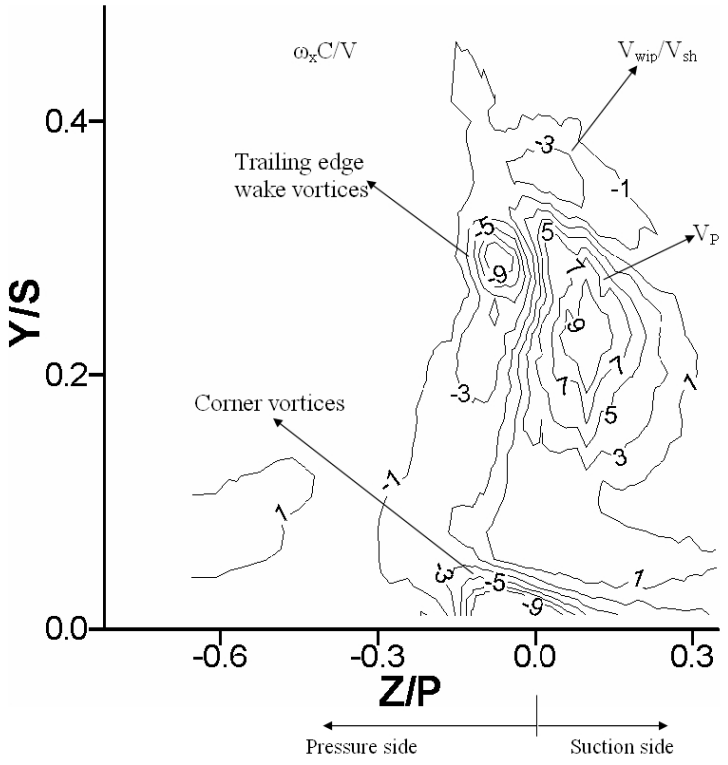

Fig. 13. Axial vorticity downstream of passage exit in a linear blade cascade. V_p= passage vortex, V_{sh}=suction side leg vortex, and Vwip= wall vortex.

Source: See Note 56 (Acharya).

Note that the passage vortex center in both the vector and vorticity plots moves farther away from the endwall (Y/S=0.0 location) as the passage vortex travels from location H to I in figure 12. This is also consistent with the flow visualization in figure 11. The axial vorticity magnitudes of the passage vortex in plane I are somewhat smaller than those in plane H. The flow turns further away from the axial direction in plane I resulting in smaller component of vorticity in the axial direction. However, the axial vorticity of the wall vortex increases in plane I as the intensity of this vortex grows as it is driven along with the passage vortex. The high negative axial vorticity at the bottom left corner in plane I in figure 12 indicates the suction side corner vortex[34]. The corner vortices are less likely to develop if the blade surface-endwall corner is filleted.

The induced wall vortex, corner vortices, and additional vortices due to the trailing edge wake can be clearly identified in the flow downstream of a blade passage as in figure 13. The data are obtained from the same passage flow as in figure 12, but the location of the data is in a pitchwise plane, K, slightly downstream of the passage exit. The projection of the trailing edge at this plane is located at Z/P=0.0 and the axial direction is into the plane of the data. The positive axial vorticity and the negative axial vorticity just above the positive region in figure 13 also indicate the passage vortex and wall vortex, respectively. The locations of these vortices are even higher above the endwall compared to those in figure 12. In figure 13, the negative trailing edge wake vorticities on the left of the passage vortex form due to the wake in the adverse pressure gradient region at the trailing edge (see figure. 3). The corner vortices indicated by the negative vorticities about Z/P=0.0 and just above the endwall are enhanced by the trailing wake flows at this location.

Figure 14 shows the influences of the various vortex structures on the flow orientation near the exit plane of a blade passage[35]. The uniformity of the flow angles near the suction side is severely affected by the vortex flow. Both the pitch and yaw angles in figure 14 are referenced to the axial +X direction. The blade turning angle at this location is about 65 degree. The positive pitch angles in the figure indicate that the flow is directed away from the endwall while the negative pitch angles indicate that the flow is directed toward the endwall. The under-turning of the flow yaw angles, which is less than 59 deg near Y/S=0.20, is very high near the passage vortex center. The high over-turning of the flow yaw angles, which is greater than 69 degree near Y/S=0.25, in the vicinity of the suction side occur because of the wall vortex or suction side leg vortex. The over-turning of the yaw angles also occur in the endwall boundary layer region at Y/S<0.12 where the cross-flow is very strong (see figure.4). Such under- and over-turning of the exit flows affect the blade loading and aerodynamic losses in the next row of blades in the turbine stage.

4.3-5 Pressure Loss

The vortex structures are a significant source of pressure or aerodynamic losses across the blade passage. They entrain fluid from the free stream flow and enhance convective turbulent transport in the endwall region as well

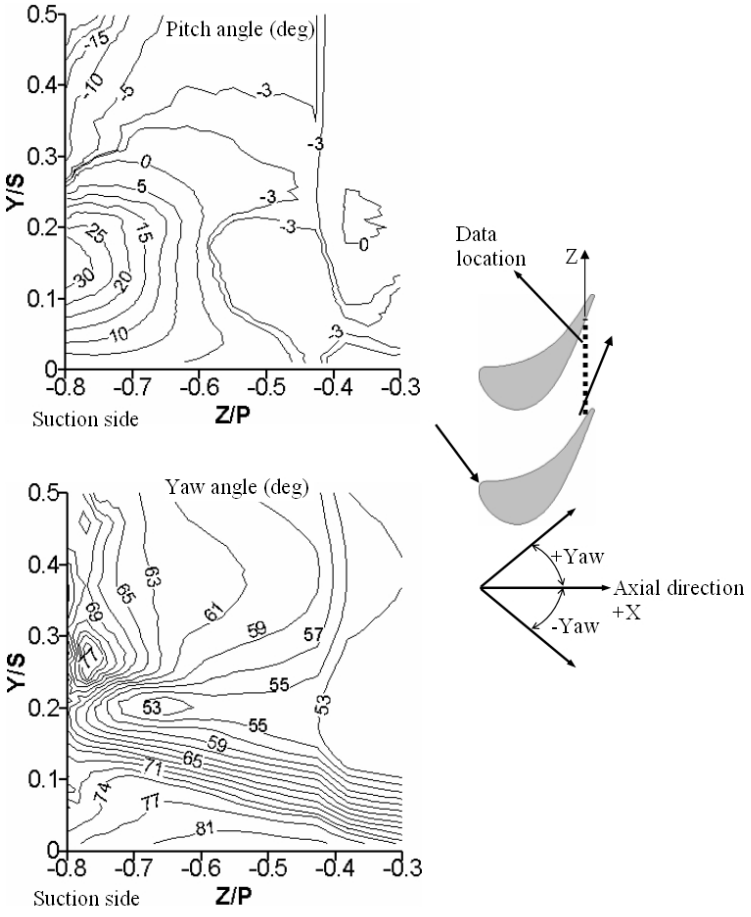

Fig. 14. Flow turning angles in a plane near exit of a blade passage.

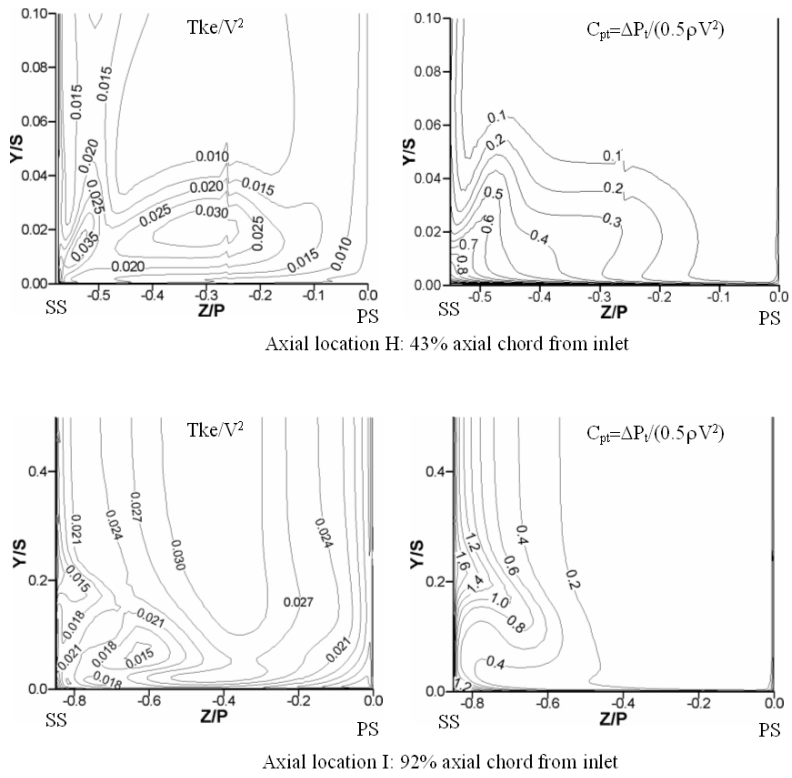

Fig. 15. Turbulent kinetic energy (Tke) and total pressure loss coefficient Cpt along a blade passage. SS=suction side, PS=pressure side, and $\Delta P_t = P_t - P_{ref}$.

Source: See Note 25 (Saha).

as on the blade surface. This also results in high local thermal loading on the turbine passage walls. Figure 15 shows the turbulent kinetic energy and total pressure loss generated by the secondary vortices at two axial locations of the blade passage of figure 12. The total pressure loss is determined from the difference of local total pressure and the reference total pressure at the passage inlet. The axial locations of figure 15 correspond to the pitchwise planes H and I in figure 12. At Z/P<-0.30, in plane H, the magnitudes of Tke/V^2 larger than 0.020 and C_{pt} larger than 0.30 can be considered to be located within the secondary vortex flow region. In plane I, the secondary vortex flow region is represented by the contours of Tke/V^2 and C_{pt} for Z/P<-0.50. Turbulent kinetic energy decreases from the axial location H to the location I in the secondary vortex flow region because the flow accelerates as it travels downstream. Because of its size and the magnitude of the vorticity, the passage vortex is primarily responsible for the turbulent kinetic energy and the total pressure losses in the secondary flow region near the suction side. Note that in both the axial locations of figure 15 the high turbulent kinetic energy just above the endwall and outside the secondary flow region occurs because of the boundary layer flow. Also it is important to realize that in the axial location I near the exit plane, the total pressure losses in the passage vortex core region are more than five times the total pressure losses in the free stream region with C_{pt}<0.20.

4.3-6 Aerodynamics of 2-D Vane Cascade

The results presented so far on the flow structure in a blade passage are very typical of other linear blade cascade studies reported[36]. The magnitudes of the flow quantities are different from one study to the other, but the pattern and arrangement of the secondary flows are similar. The secondary flow patterns in a two-dimensional vane cascade are also expected to be similar to that in a linear blade cascade. This is because the formation of the leading edge horse-shoe vortex is inevitable for the vane passage as well. The horse-shoe vortex is then driven by the endwall cross flow and pressure gradient in the passage forming the suction side leg and pressure side leg vortices. The secondary flows are weaker and smaller in a linear vane passage than in a linear blade passage because of the smaller flow turning and weaker endwall cross flow in the vane passage[37]. However, the same components of the secondary flows are present in both the vane and blade passages. Due to the weaker secondary flows in the vane passage, the pressure losses are smaller relative to those across a blade passage. Figure 16 presents the data measured in a linear vane cascade[38]. The pressure side leg vortex (clockwise rotating) and the suction side leg vortex (counter-clockwise rotating) at plane SS-1 in figure 16 are located near the pressure side and adjacent to the suction side of the vane, respectively. At a farther downstream location SS-3, the pressure side leg vortex is driven close to the suction side and pair up with counter-rotating suction side leg vortex to form the passage vortex. Like the blade passage flow, the suction side leg

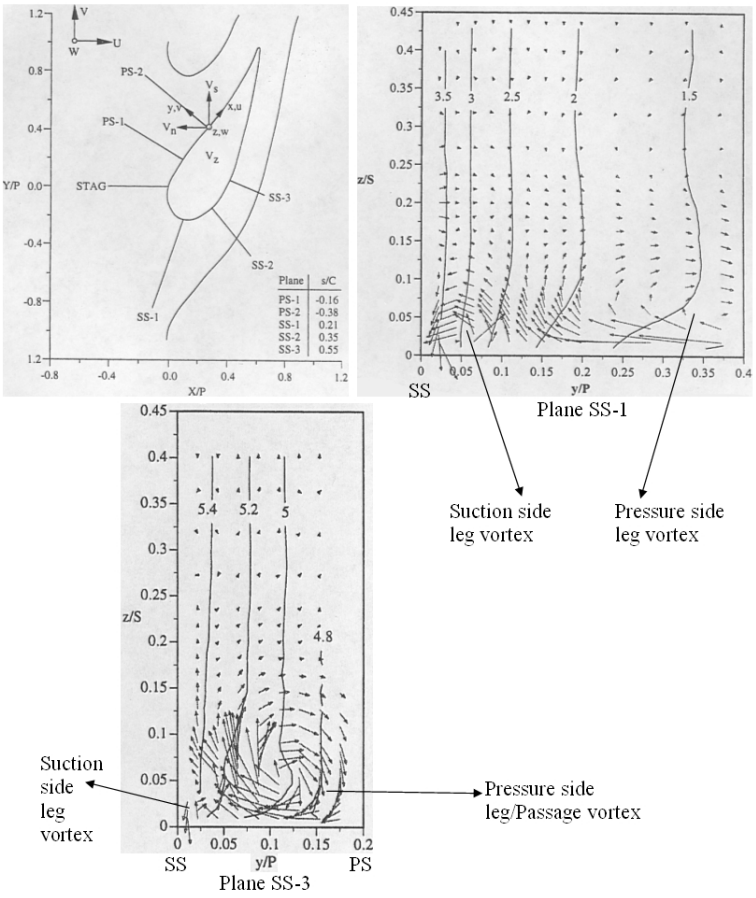

Fig. 16. Secondary velocity vectors and streamwise velocity contours showing vortex flow formations in a linear vane cascade. SS= suction surface and PS= pressure surface.

Source: See Note 33.

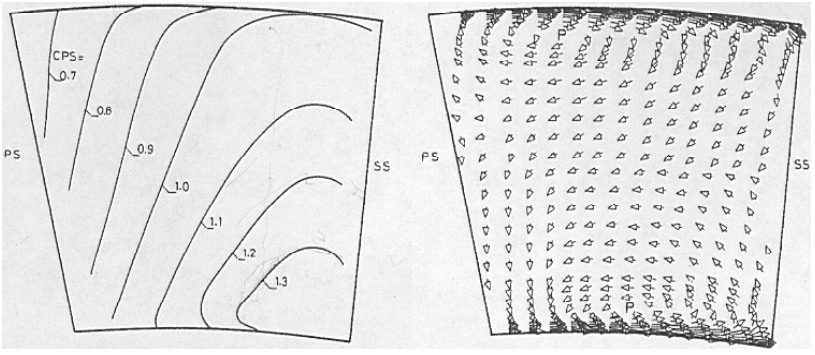

Fig. 17. Static pressure and secondary velocity vectors across a plane in a vane passage of annular cascade. PS=pressure side and SS=suction side.

Source: See Note 3. (Sieverding)

vortex clearly appears much weaker and smaller than the passage vortex at this location in the vane passage. However, the relative arrangement of the passage vortex and suction side leg vortex at SS-3 in figure 16 is different than that observed at plane H in figure 12. The evolution of the passage vortex structure along a linear vane cascade and downstream of a linear vane passage show qualitative similarity with those found in figures 12, 13, and 16[39].

4.3-7 Aerodynamics of 3-D Cascade

A three-dimensional cascade is usually formed when the linear or twisted blade or vane profiles are stacked in an annular passage. Thus, the flow area in the cascade passage increases from the hub side to the tip side of the adjacent blades. Because of this passage structure, a radial pressure gradient is added to the flow everywhere in the annular passage[40]. This radial pressure gradient directing towards the hub neutralize the radially outward centrifugal force experienced by the free-stream fluid which is in equilibrium across the annular passage. The radial pressure gradient increases from the pressure side to suction side[41]. The data in figure 17, adopted from Sieverding et al., show the static pressure coefficients and secondary velocity vectors across an axial plane slightly upstream of the passage exit of an annular vane cascade. In the figure, the difference in static pressure coefficient between the hub and casing is higher on the suction side than on the pressure side. The effects of such pressure gradients are greater at the passage exit than within the passage. The vectors show the formation of the passage vortex near the hub and casing side. The radial displacement of the vortex centers are mostly the consequence of the pitchwise cross flow rather than the radial pressures as observed in a linear cascade. The total pressure losses near the hub and casing walls due to the two passage vortex structures are also nearly identical. However, in the same study, the total pressure losses at the passage exit are found to be asymmetric with respect to the spanwise meridian unlike that observed across a linear cascade. The total pressure losses downstream of the cascade are considerably higher near the hub wall than those near the casing[42]. This is attributed to the influence of the radial pressure gradient. Near the endwall in the passage, the streamwise velocity decreases in the boundary layer and the secondary flow region. As a consequence the centrifugal force generated from the circumferential component of the streamwise velocity decreases near the endwalls. But, the radial pressure gradient remains unchanged. Thus, the non-equilibrium behavior near the casing results in the reduced total pressure loss there.

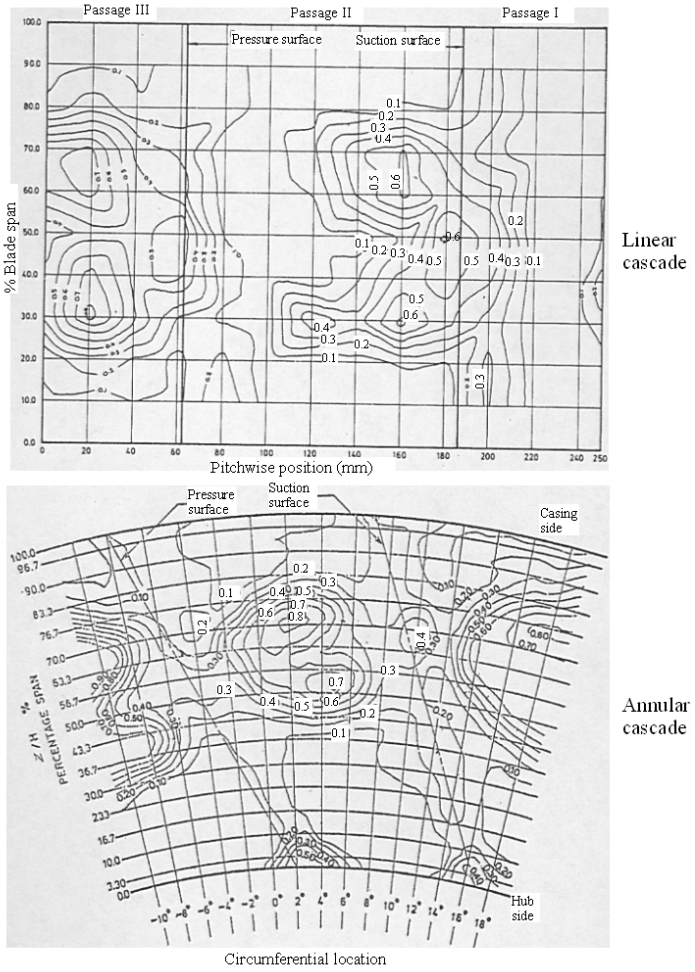

Fig. 18. Total pressure loss coefficients at exit plane of a linear and an annular cascade.

*Source: See Note 13.** (Moustapha)

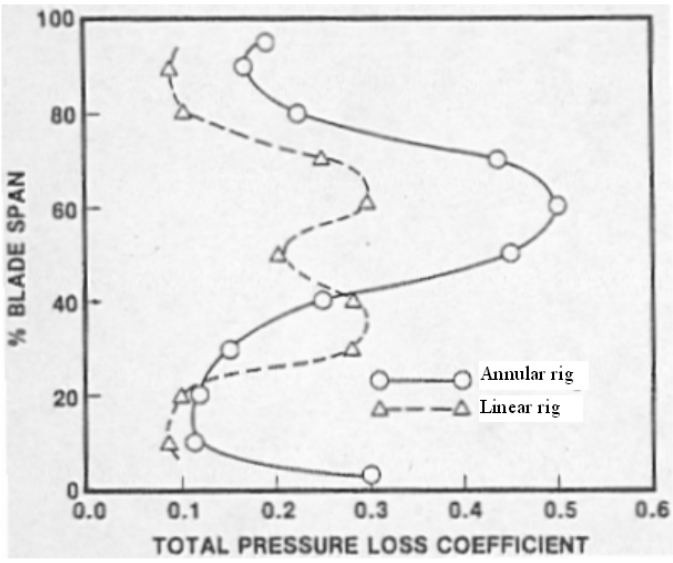

Fig. 19. Spanwise distribution of pitchwise averaged total pressure loss coefficient for linear and annular cascades in Fig. 18.

*Source: See Note 13.** (Moustapha)

*The original version of this material was published by the Advisory Group for Aerospace Research and Development, North Atlantic Treaty Organization (AGARD/NATO) in AGARD Conference Proceedings CP-469 "Secondary Flows in Turbomachines" in 1990.

A comparative study of a linear cascade and an annular cascade with the same two dimensional blade geometry employed is presented in figure 18[43]. The total pressure losses in figure 18 are obtained at the same exit location relative to the blade trailing edge in the two passages. It is clearly evident from the plots that the radial pressure gradient in the annular cascade plays a significant role and alters the pressure loss distribution when compared to the linear passage which experiences no such pressure gradient. The pressure losses in the linear cascade have two distinct high loss regions, located symmetrically about 50% blade span, near the suction surface. These are the signatures of passage vortices from the top and bottom endwalls. In contrast, the annular cascade has one high total pressure loss region between 48% and 77% span. In this loss region, the peak losses are 0.70 and 0.80 at 53% and 70% span, respectively, indicating that the cores of the hub side and casing side passage vortices are very close to each other.

The plots in figure 19 determined from the local data in figure 18 compares the pitchwise averaged total pressure loss magnitudes between the linear cascade and the annular cascade. The two peaks in figure 19 for the planar cascade are a consequence of the distinct passage vortex pair observed in the local data. For the annular cascade, one peak in the average pressure loss distribution occurs because of a single high pressure loss region in the local data. In general, the average total pressure losses are much higher for the annular cascade than for the linear cascade along most of the span. Between 20% and 40% span at the inner endwall side the average losses are higher for the linear rig as the passage vortex from this endwall is located in this region.

The static pressure distributions on the annular endwalls as shown in figure 20 indicate different distributions for the casing wall and hub wall. The pitchwise pressure gradient extends all the way down to the trailing edge for the casing wall. While the cross pitch pressure gradient for the hub wall is high in the first half of the passage, the gradient decreases significantly in the latter half of the passage compared to that for the casing. Such pressure distributions provide the radial pressure gradients between the two endwalls in the annular cascade which is responsible for the radial movement of the secondary flows as explained previously. The magnitudes of the static pressure coefficient near the suction side in figure 20 are higher for the hub wall than for the casing in the first half of the passage. In the second half of the passage, these magnitudes near the suction surface are higher for the casing wall. Thus, the endwall cross flow covers most of the casing wall, while it covers only the first $\frac{2}{3}$rd of the hub wall. Note the qualitative similarity of the contour distributions between the linear passage endwall (figure. 6) and annular passage casing wall (figure 20).

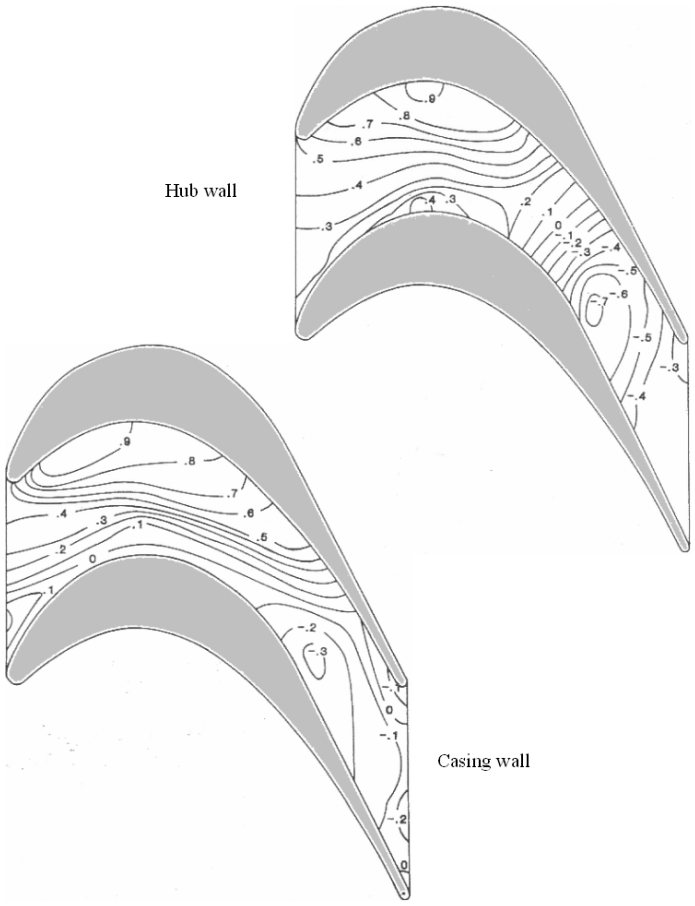

Fig. 20. Static pressure coefficients on endwalls in a blade passage in an annular cascade.

*Source: See Note 13.** (Moustapha)

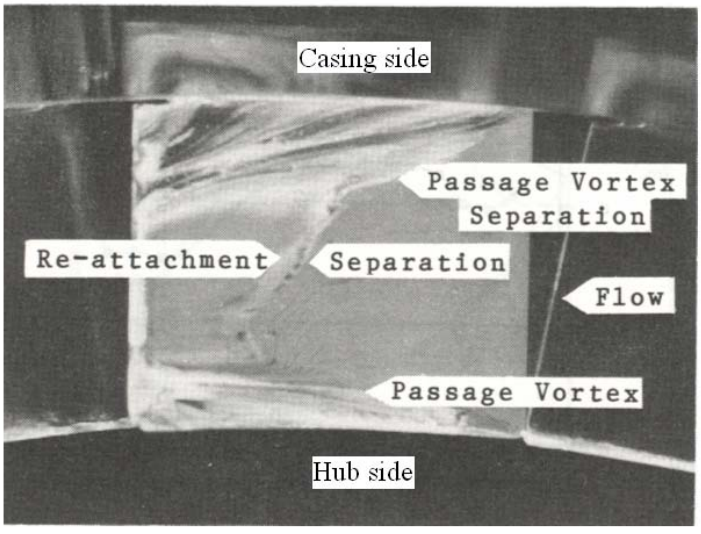

Fig. 21. Surface flow visualization on a vane suction surface in an annular cascade.

Source: See Note 45.

*The original version of this material was published by the Advisory Group for Aerospace Research and Development, North Atlantic Treaty Organization (AGARD/NATO) in AGARD Conference Proceedings CP-469 "Secondary Flows in Turbomachines" in 1990.

Blade surface pressure distributions on the pressure surface are about the same for the annular cascade and linear cascade[44]. The radial pressure gradient on the pressure surface (annular cascade) is present only near at the hub side. On the contrary, the radial pressure gradient is present along the entire span on the blade surface and is larger in the first one-third of the surface in axial direction compared to the rest of the surface. When compared at the same corresponding radial location, the magnitudes of static pressure coefficient on the suction surface are always higher in the annular cascade than in the linear cascade due to the radial pressure gradient. However, the suction surface pressure coefficient distributions in the axial direction follow similar patterns in both types of cascade employing same blade geometry. Thus, the two dimensional local separation bubbles also appear on the blade suction surface in an annular passage.

The vane suction surface flow pattern in an annular cascade is presented in figure 21[45]. The visualization reveals the asymmetric surface streamlines relative to the spanwise meridian unlike the streamline patterns on the suction surface in a linear cascade. In figure 21 also, the separation lines divide the near surface flow behavior into three regions as has been observed in case of a linear passage. The first region is the two dimensional laminar region extending from the leading edge to the inclined separation line (spanwise) between passage vortex separation lines. In the radial/spanwise direction this region is limited between the separation lines for passage vortex. Near surface flow simply follows the suction surface in the first region. The second region is the turbulent flow region that extends behind the inclined re-attachment line to the trailing edge in figure 21. Unlike that in the linear cascade (figure 7), the suction surface separation bubble formed here (figure 21) by these inclined separation and re-attachment lines is asymmetric. The third flow region, which is the three dimensional boundary layer region in figure 21 limited by the passage vortex separation line and endwall, is larger on the casing side than on the hub side. The separation lines extend all the way to the trailing edge. The separation line for the passage vortex at the casing is farther away from the casing than the separation line for the hub-end passage vortex line is from the hub wall. This is in accordance with the passage vortex movement observed in figure 18 for the annular cascade and as described, is caused by the radial imbalance of the radial forces. The inclination of the surface streamlines in the third region caused by the passage vortex funneling and entrapping fluid is an indication of the vortex strength.

The three dimensional vortex flows near the hub and casing walls are enhanced in an annular rotor passage where the blades rotate relative to a stator passage. In the blade stage, there is a gap between the blade tip and casing to allow for rotation. Due to the pressure gradient from the blade pressure side to the suction side there is a leakage flow from the pressure side to the suction side in the tip gap. The tip-gap flows generate an additional vortex flows near the casing wall which develop and grow along with the casing side passage vortex in the rotor passage. The tip vortex influences the passage vortex from the casing wall. Figure 22 shows the tip-clearance vortex and passage vortex structures near

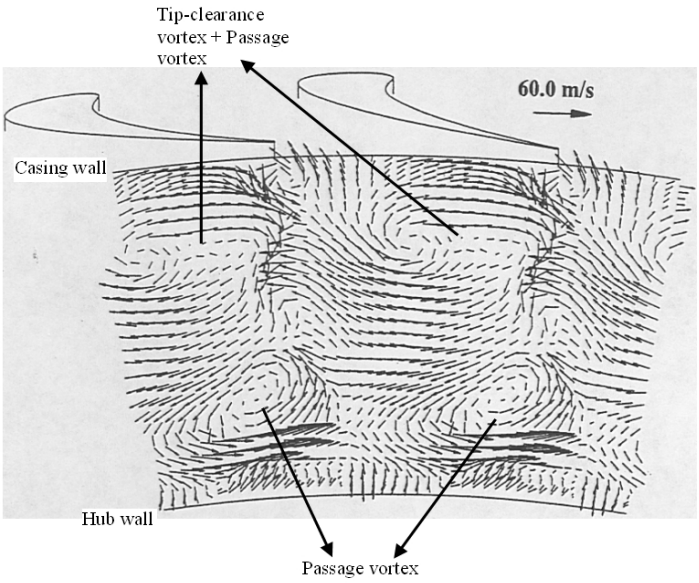

Fig. 22. Measured secondary velocity vectors at rotor exit in an annular passage.

Source: See Note 3. (Gallus)

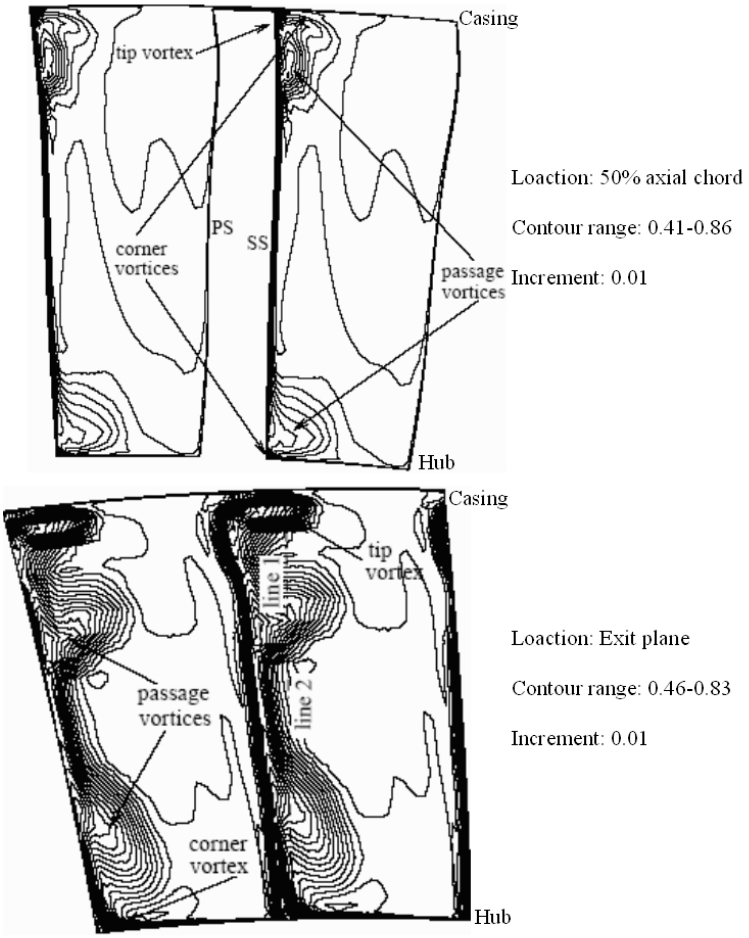

Fig. 23. Relative total pressure contours in an annular rotor passage showing vortex flows. PS= pressure side and SS= suction side.

Source: See Note 47.

the casing wall and hub wall at the exit plane of a rotating rotor passage. As indicated in the figure, the counter-rotating secondary flows in the passage vortex near the casing wall are caused by the influence of the tip vortex. According to Gallus et al., the flow interactions between the rotor-stator rows change the static pressure distributions on the rotor surface periodically[46]. The isobar contour lines in figure 23 show that the tip-clearance vortex strengthens the radial inward movement of the casing passage vortex in a rotor passage[47]. This occurs as the tip vortex grows and intensifies along the passage and pushes the passage vortex in the radial direction. The size and strength of the passage vortices formed in the rotor passage fluctuate depending on the position of the trailing edge wake and passage vortices from the stator row. When the stator wake and passage vortices hit the rotor blade leading edge, the passage vortices in the rotor passage grow larger and stronger. At the rotor exit, the locations of the passage vortices and trailing edge wake also fluctuate depending on the wake and vortices from the upstream stator row[48]. The tip-clearance vortex increases the suction side static pressure and decreases the pressure side static pressure at the tip region of the rotor blade. This reduces the blade loading at the tip region in the rotor stage.

4.3-8 Aerodynamics With Passage Modifications

Recently there have been a number of studies directed at structural modifications of the blade passage with the aim of reducing the secondary flows in the passage. The secondary flows are the significant sources of aerodynamic losses and increased thermal loading in the passage walls. The large passage vortex structure also makes the exit flow turning non-uniform across the entire passage exit plane. This subsequently increases the noise level, secondary losses, and fluctuations of the blade loading on the following blade row. Cold air is injected through tiny holes in the endwall to provide a protective film on the endwall from the hot gas in the passage main flow. The effectiveness of film cooling is adversely affected by the secondary flows in the endwall. The coolant air injected from the holes located upstream of and adjacent to the separation line (figure 4) is lifted up from the endwall by the passage/pressure side leg vortex and suction side leg vortex. This exposes a large part of the endwall immediately downstream of the separation line to the hot gas. The wake and exit passage vortices also affect the coolant flow injected from the holes located in the platform between the two stages. The non-uniformity in the exit flow angles alters the expected trajectories of these coolant paths. The structural modifications of the passage are undertaken at or near the endwall that only affects the flow in the boundary layer and, beneficially alters the secondary flow behavior. Therefore the blade profile remains unchanged for most of the blade span, and only the minimum change occurs in the blade loading. The geometrical modifications are still the subject of ongoing investigations and include leading edge fillet additions and endwall profiling. In the discussion below, attention will be focused on these two.

Leading Edge Fillet: This modification is also termed as the leading edge contouring near the endwall. Fillets are placed at the junction of the leading edge and endwall. Several forms

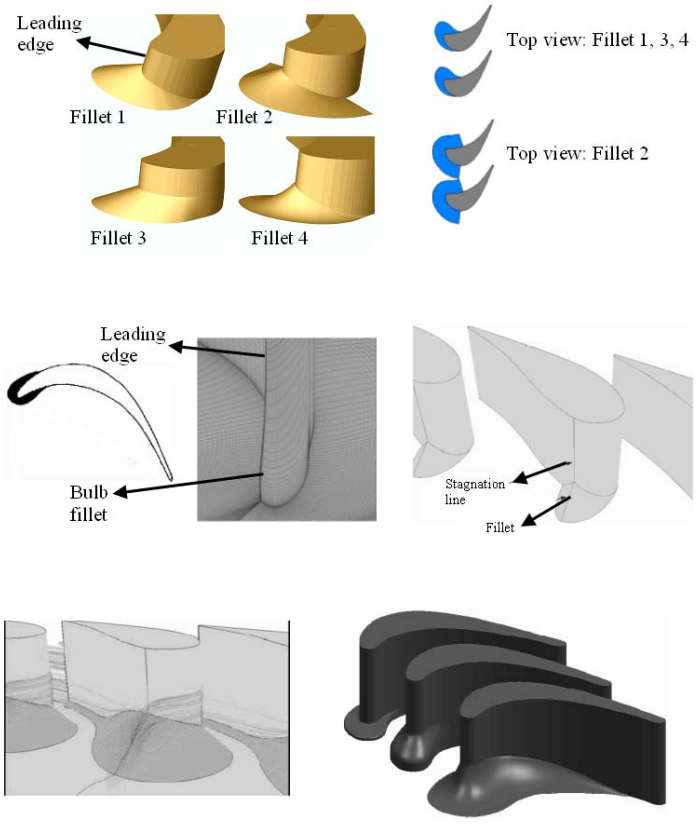

Fig. 24. Different leading edge fillet profiles employed in aerodynamic loss reduction studies

Source: See Notes 22, 25, 49.

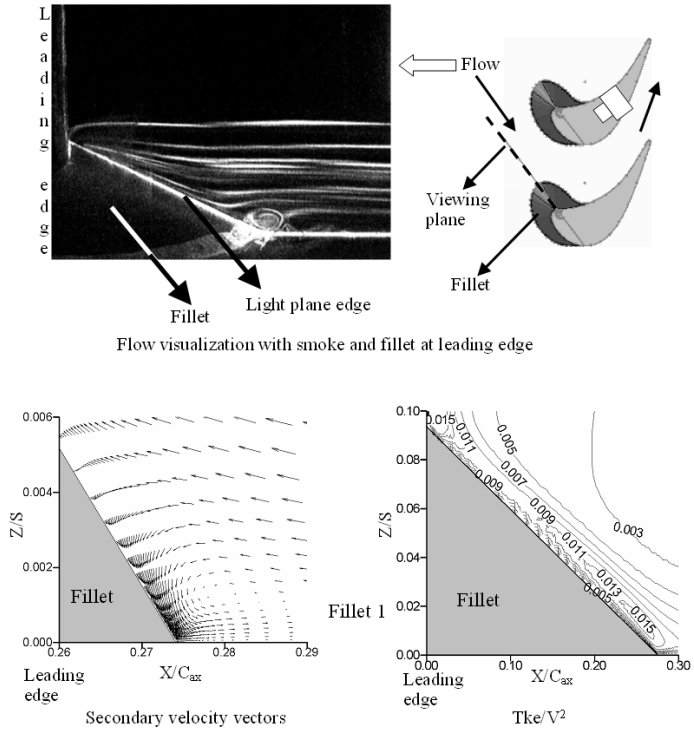

Fig. 25. Leading edge horse-shoe vortex in a linear blade passage with leading edge fillet. Tke= turbulent kinetic energy.

Source: See Notes 22, 25.

of the fillet profiles have been tested and are shown in figure 24. As can be seen in the figure, two types of basic construction of fillet profiles can be identified: (i) profile with varying height from the blade surface to the endwall and (ii) profile of bulb with surface thickness at the outer periphery[49]. The thickness of the type (i) fillet profiles reduces to zero as they extend out from the blade surface to the endwall. These fillets may blend with either the endwall or blade wall or with both the endwall and blade surface as they wrap around the leading edge extending inside the passage. The fillet profiles of the type (ii) blend with the blade surface as they wrap around the leading edge, but meet the endwall with a finite thickness. Type (ii) fillets simply thicken the blade profile near the leading edge at the endwall. All types of fillets studied until now have asymmetric profile with respect to the leading edge and have their highest point located at the leading edge. The height of this highest point from the endwall i.e. the maximum height of the fillets is typically one boundary layer thickness of the incoming flow.

The studies mentioned above show that type (i) fillets are the most effective in reducing the secondary flows in the blade passage. These fillets reduce the size and strength of the leading edge horse-shoe vortex. Consequently, the strength of the passage vortex is reduced. The high total pressure losses due the passage vortex then also decrease across the blade passage. Figure 25 shows the horse-shoe vortex structure at the leading edge with a fillet profile of type (i) employed at the leading edge. The profile height varies linearly to zero from the blade surface to the endwall and blends with the endwall and blade wall inside the passage on the pressure side and suction side (Fillet 1[50]). The blade passage is the same as that in figure 8. The wedge shaped object on the left of the flow visualization image of figure 25 is the fillet profile. The size of the horse-shoe vortex is about half in the flow visualization and about one-fifth in velocity vector plot with the fillet compared to the case without any fillet. Note that the flow visualization is observed at a low speed to avoid any smearing and diffusion of smoke. The flow area at the leading edge is reduced in the passage with the fillet. For the incompressible flow, this will cause the boundary layer fluid to be displaced from the leading edge plane. Also, the adverse pressure gradient along the leading edge plane (due to the stagnation) is reduced by the fillet slope. All these factors are responsible in reducing the size of the horse-shoe vortex with the fillet. The turbulent kinetic energy is also reduced significantly in figure 25 compared to what is observed without the fillet. This indicates that the strength of the horse-shoe vortex is also reduced by the fillet. There is also no apparent structure of the leading edge corner vortex in the secondary velocity vectors with the fillet.

As the horse-shoe vortex is reduced, the Fillet 1 is expected to reduce the passage vortex size and strength downstream in the blade passage. Figure 26 shows the passage vortex at a plane 92% axial chord (near the exit) with and without fillet in the same blade passage. Comparing the velocity vectors in figure 12 (Plane I) and figure 26, it can be seen that the location of the passage vortex center with the Fillet 1 moves little higher above the endwall than without the fillet. In an upstream location near the suction side in the blade passage, the suction side leg vortex is reduced in size and weakens with the Fillet 1 compared to that without the fillet[51]. The significant differences are observed in the total pressure loss contours of figure 26. The high total pressure loss region (C_{pt}>0.45) can be considered as the signature of the passage vortex. The C_{pt} contours presented here are measured

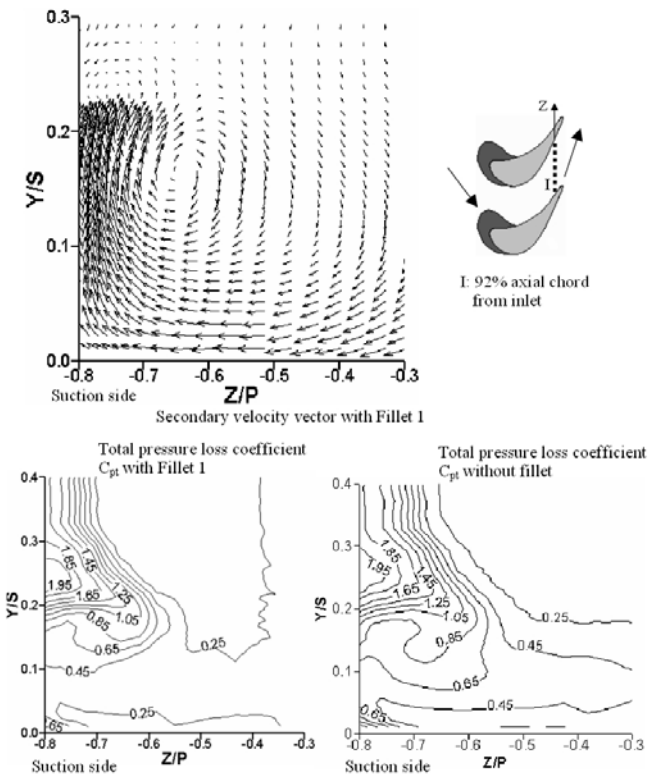

Fig. 26. Passage vortex and total pressure loss at 92% axial chord with and without fillet.

Source: See Note 25.

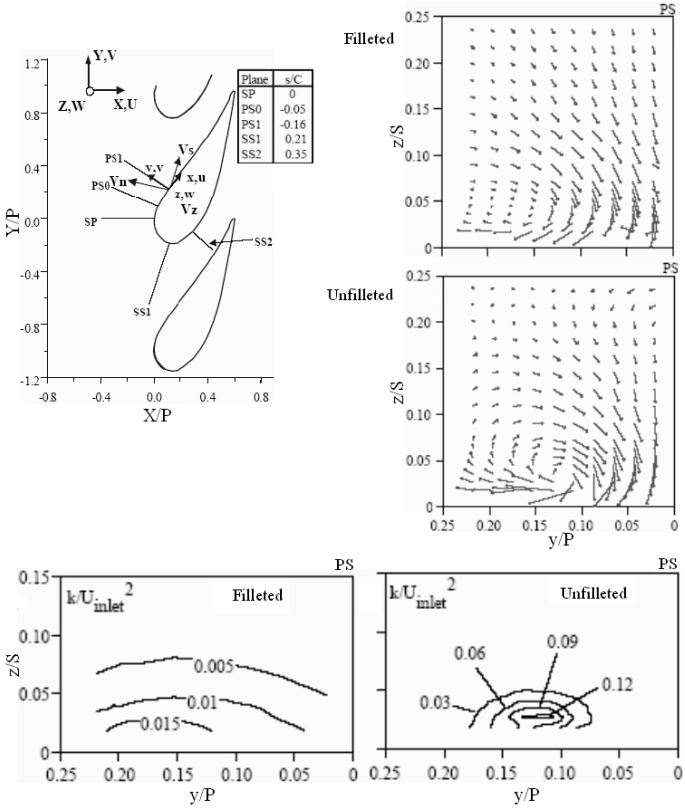

Fig. 27. Secondary velocity vectors and turbulent kinetic energy (k) at pressure side (Plane PS1) of a linear vane cascade with and without fillet. PS= pressure side.

Source: See Note 49. (Zess)

with a five-hole pneumatic probe unlike the magnitudes in figure 15 which are obtained from computations in the same passage with an incoming boundary layer of smaller thickness. The total pressure losses in figure 26 are much lower at the bottom part of the passage vortex with the fillet than without the fillet. This indicates that the Fillet 1 has reduced the passage vortex both in size and strength. Also revealed, the under-turning (yaw angle) of the exit flow with the Fillet 1 occurs over a larger region in the passage vortex core[52]. Similar results about the passage vortex and associated total pressure losses are observed with other fillet profiles of type (i)[53]. Figure 27 shows the effectiveness of another fillet profile of type (i) in reducing the passage vortex in a linear vane cascade. The quantities in figure 27 are measured in a plane normal to the vane pressure surface[54]. The velocity vectors in the figure show the structure of the pressure side vortex near the pressure surface. As can be clearly seen, the pressure side leg vortex is not complete for the filleted vane unlike the vortex for the unfilleted case. The spiral of the vortex is not complete in the same location for the filleted case as the passage vortex is weakened. This will eventually make the passage vortex weaker down the passage for the filleted vane. Also, the location of the passage vortex center appears to shift farther away from the pressure side for the filleted case compared to that for the unfilleted case. The turbulent kinetic energy magnitudes in figure 27 are much smaller for the filleted vane than those for the unfilleted vane. The k-contours indicate a well-defined vortex core for the unfilleted case while the k-contours for the filleted case are much uniform in the y/P direction. The fillet causes the passage vortex in this plane to fluctuate along y/P as the velocity component in this direction has the largest fluctuations with the fillet. On the contrast, the large fluctuations in the w-velocity component cause the passage vortex to fluctuate in the z/S direction for the unfilleted vane.

Endwall Profiling: Endwall profiling is achieved in two ways- axial profiling along the passage with no pitchwise variation and non-axisymmetric profiling along the passage with profile variations in both the axial and pitchwise directions. The profiling is aimed either to accelerate the boundary layer fluid at the endwall or to reduce the pitchwise pressure gradient at the endwall.

(i) *Axial Profiling of the Endwall*: Since there is no variation of the profile in the pitch direction, this profiling is also termed as the two dimensional axisymmetric contouring. The profiling is employed on either of the endwalls in the passage, but not on the both endwalls. The height of the profile increases over a smooth curve from the leading edge to the trailing edge such that aspect ratio of the exit plane or the throat area is unaffected as shown in figure 28. This type of endwall profile was studied in linear vane passages[55]. The axisymmetric profiles of the endwall upstream of the blade/vane passage such as the profile (b) of figure 28 are also studied[56]. Upstream profiles in the first stage nozzle guide vane are used for the gas path transition from the combustor chamber to the turbine inlet. In any profile shown in figure 28, the inlet velocity to the blade/vane passage decreases (due to increased passage area) and the flow acceleration through the passage increases (due to decreased passage area). This leads to a reduction in the boundary layer thickness and suppresses the growth of secondary flows on the endwalls. Also, the exit flow angle is expected to undergo less under-turning and over-turning due to the higher flow acceleration downstream with the endwall profiling extending through the passage.

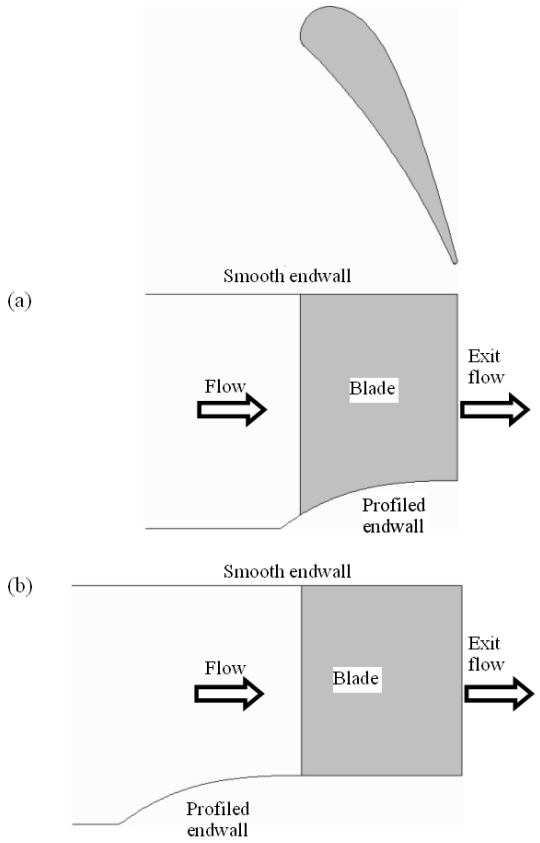

Fig. 28. Axisymmetric axial profiling of endwall: (a) endwall profile through blade passage, (b) endwall profile upstream of blade passage.

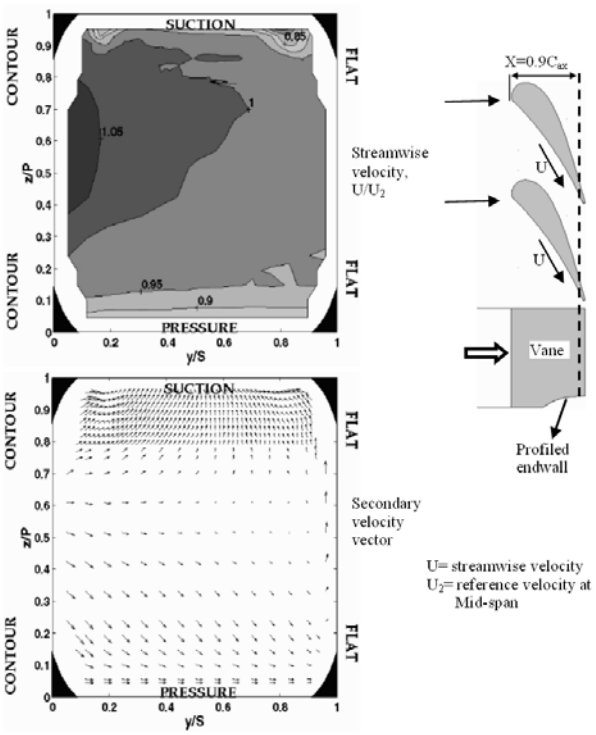

Fig. 29. Streamwise velocity and secondary velocity vectors at 0.90Cax in a linear vane passage with endwall profiling through passage aft.

Source: See Note 55. (Burd)

Figure 29 shows the effects of the endwall profiling through the passage aft of a vane cascade on the secondary flows[57]. The data are presented in a plane near the passage exit where the endwall profile has become almost flat. The low streamwise velocity magnitudes adjacent to the pressure side in figure 29 are located within the boundary layer on this side. The high velocities near the contour endwall are the results of flow accelerations along the endwall. The two concentrated low velocity regions (U/U_2<0.90) adjacent to the suction side near the flat and contour endwalls are located in the passage vortex at this plane. The passage vortex region near the contour endwall is about half the size of that near the flat endwall. The velocity vector plot in figure 29 reveals that fluids are being displaced from the contour endwall region toward the mid-span (y/S=0.50) as all the vectors in this region are pointing toward the mid-span. The vectors pointing toward the suction side near y/S=1.0 indicate that the cross-pitch flow is much stronger at the flat endwall than at the contour endwall. As this component of the flow is one of the major contributors for the growth of the passage vortex, the passage vortex is smaller near the contour endwall. The passage vortices can be identified by the small turning vectors creating an apparent clockwise and counter-clockwise motion near the contour endwall and flat endwall, respectively. The static pressure distributions near the endwalls along the passage in figure 30 illustrate further the effects of the profiled endwall on the cross-pitch and secondary flows. The contoured profile for the data in figure 30 is similar to that in figure 29 except the profile now extends across the entire passage length. The other endwall of the passage is flat without any contouring. In figure 30, the pressure distribution at the flat wall is similar to what is observed on the non-profiled endwalls in a linear vane passage. At the contoured endwall side, the contour lines of constant pressure near the leading edge are aligned more in the pitch direction than in the axial direction. In contrast, the constant pressure lines at the flat wall side near the leading edge are aligned more in the axial direction. The pressures at the contoured endwall are higher than those at the flat endwall for the first 40% axial chord. The pressures then are lower at the contoured endwall than at the flat endwall for the latter 60% axial chord. Thus, the pressure gradient at the contoured endwall is more parallel to the vane surface than to the pitch direction. The pressure gradient at the flat endwall is more parallel to the pitch direction than to the vane surface. As a consequence, the cross flow in the pitch direction is stronger on the flat endwall than on the contoured endwall. The reduced strength of the endwall cross flow then suppresses the growth of the passage vortex as mentioned earlier.

The total pressure loss at the passage exit is reduced when the passage vortex near the contoured endwall is weakened and reduced in size. This is illustrated in the total pressure measurements in figure 31[58]. The planar vane cascade in the figure employs flat endwalls at both the hub and tip while the tip wall is axially contoured and the hub wall is flat for the contoured vane cascade. The contouring here extends across the entire passage length. The data in figure 31 are presented in a plane located 10% axial chord downstream of the passage exit. Hence, the endwall profile is flat at this location and the total passage height (z/S) is same for both the planar cascade and contoured cascade. The passage vortex regions in the figure can be identified by the highly concentrated circular contour lines near the endwalls. The parallel contour lines about y/P=0.50 indicate the wake region. The loss distributions are almost symmetric about the mid-span location z/S=0.50 for the planar cascade and the passage vortices are located away from the endwall regions as expected. While the loss distributions are asymmetric in the contoured cascade, the passage vortex loss region about z/S=0.10 from the flat wall side is similar to the passage vortex loss region in the planar cascade. However, the core loss region of this passage vortex has shifted closer to the flat wall side and further away from the suction side trailing edge.

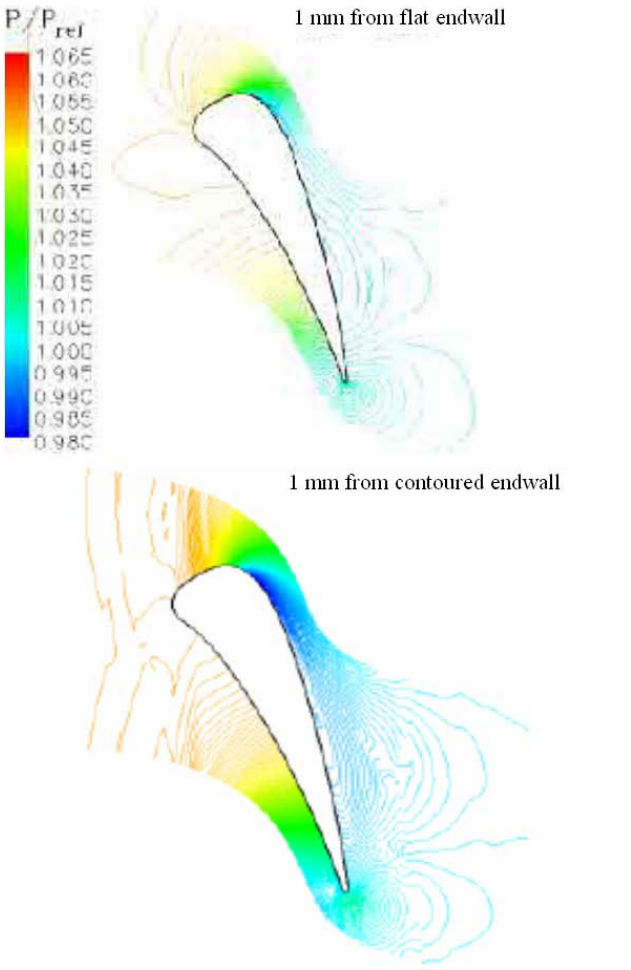

Fig. 30. Static pressure distributions near endwalls in a linear vane passage with endwall profiling extending from leading edge to trailing.

Source: See Note 55. (Shih)

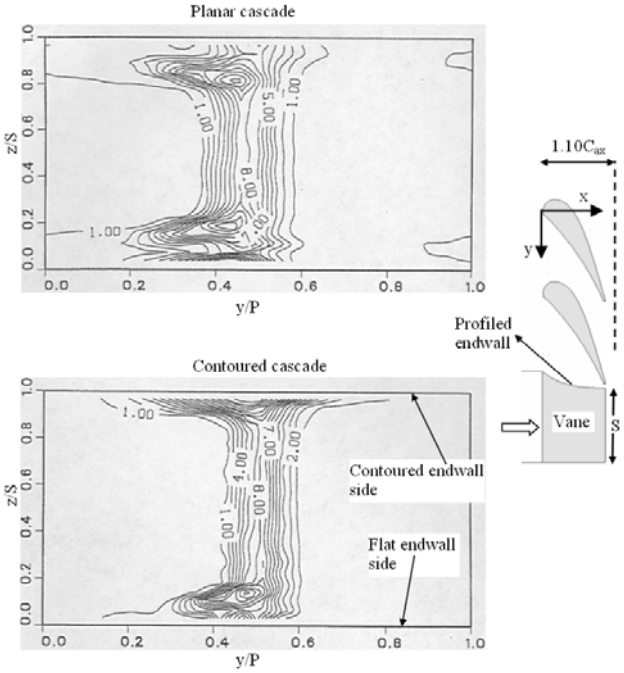

Fig. 31. Total pressure loss, Cpt distributions at 1.10Cax for a linear vane cascade with and without endwall profiling.

Source: See Note 55. (Dossena)

The loss contours due to the passage vortex from the contoured endwall side in the contoured cascade are located just adjacent to the contoured wall side at z/S=0.95. Thus, the spanwise (z/S) extent of the passage vortex at the contoured endwall side is smaller compared to those in the planar cascade. Another important difference between the two cascades is identified by comparing the wake regions. The pitchwise width of the wake region for the contoured cascade is smaller than that for the planar cascade. This can be attributed to the velocity and pressure distributions on the vane suction surface in the contoured cascade. The lowest pressure and consequently the peak velocity on the vane suction surface shifts toward the trailing edge in the presence of the contoured endwall. Thus, the diffusion rate of velocity is lower over the suction surface in the contoured cascade[59]. As a result the extent of the adverse pressure gradient region near the suction surface trailing edge decreases reducing the extent of the trailing edge wake. Thus, the profile loss in the contoured cascade also decreases.

The effect of axial profiling of endwall in an annular vane passage was measured[60]. The endwall contouring is employed at the tip wall in the last half of the passage. The contouring affects the pressure distributions significantly on the vane suction surface at the tip region. The suction surface pressure at the tip region rises in the first 50% of axial chord. In the latter 50% of axial chord, the pressure decreases on the suction surface and the maximum suction side velocity shifts toward the trailing edge at the tip region. As a result, the adverse pressure gradient on the blade suction surface is reduced at the vane tip region. In the annular flow area, the static pressure and total pressure loss distributions are affected in the latter part of the passage where the tip contouring is located. In the aft part of the passage, the radial pressure gradient directed toward the hub endwall in an annular passage with no tip wall contouring is inverted in the upper half span near the suction side when the tip contouring is employed. Unlike the annular passage without tip contouring, the radial flow angle at the exit plane is negative across most of the plane with the tip wall contouring. Downstream of the passage exit the total pressure loss region due to wake reduces in the pitch/circumferential direction significantly for the contoured annular passage (tip wall profiling) compared to that for the plain annular passage. This occurs as the adverse pressure gradient at the vane surface trailing edge reduces for the contoured tip/casing endwall. The same relative behavior for the wake region has been observed for the linear vane cascade with and without tip wall contouring[61]. At the same downstream location as above, Boletis (1985) shows that the high total pressure loss region near the contoured casing wall (annular) is also reduced compared to that near the plain annular casing wall. However, the magnitudes of the total pressure loss in this region are about the same for both type of casing walls.

(ii) *Non-axisymmetric Profiling of Endwall*: In this case, the endwall profile variations can be achieved by varying the height of the profile over a smooth curve in the axial direction and over another smooth curve in the pitch direction. The objective is to increase the endwall height near the passage pressure side and decrease the endwall height near the suction side with respect to a baseline flat endwall. The endwall region static pressure on such profile is expected to decrease near the pressure side and increase near the suction side, thus reducing the pitchwise pressure gradient and the strength of the cross-pitch flows at

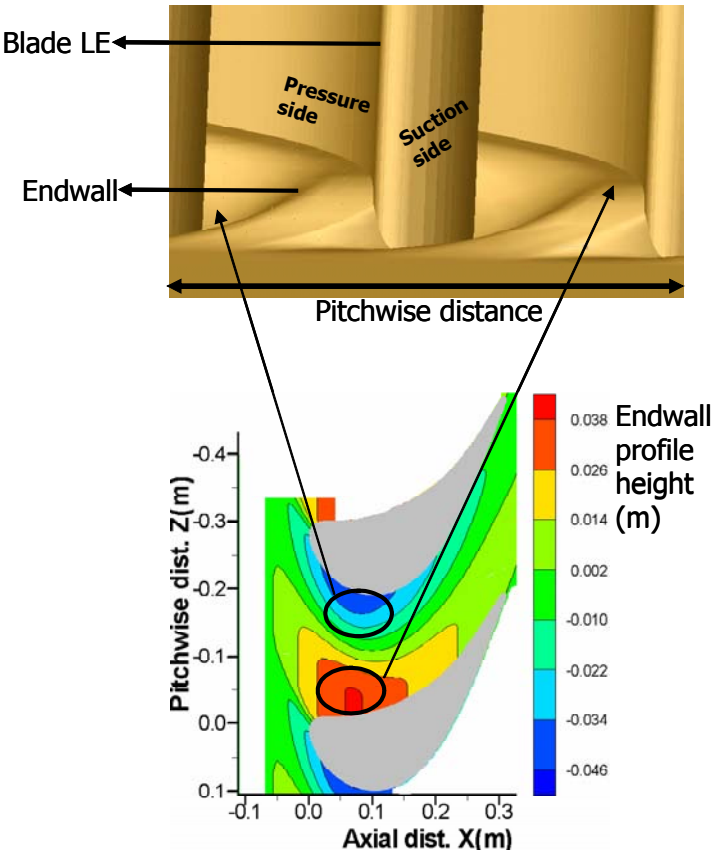

Fig. 32. Non-axisymmetric profile of endwall employed in a linear blade cascade.

Source: See Note 62.

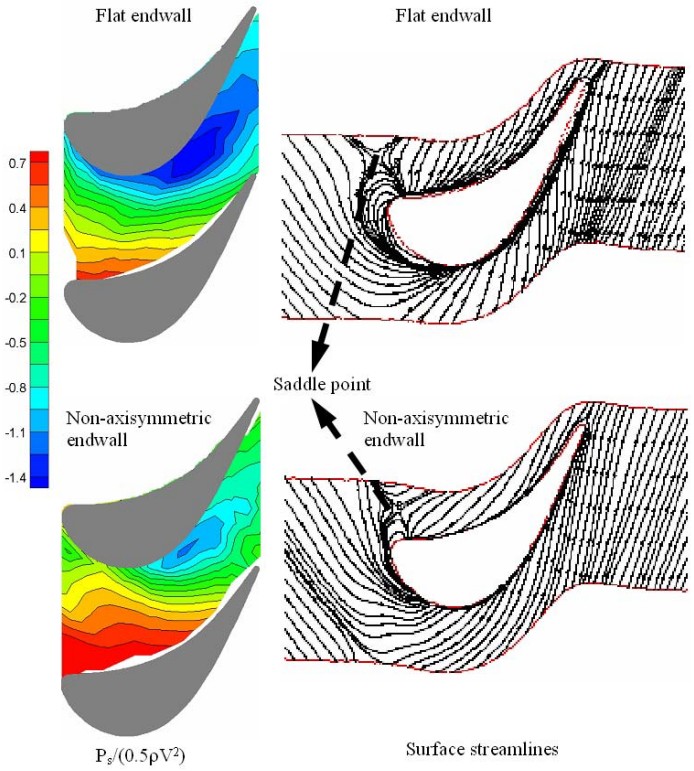

Fig. 33. Measured static pressure and computed surface streamlines at a flat endwall and at a non-axisymmetric contoured endwall in a linear blade passage. Ps= wall static pressure.

the endwall. Figure 32 shows the profile of such an endwall that is employed[62]. The figure also includes the profile height variations across the passage. Harvey et al and Hartland et al. provide guidelines for designing the non-axisymmetric contour profiles for the linear cascade[63].

The measured static pressure distributions and computed surface streamlines at a flat endwall and at the contoured endwall of figure 32 are presented in figure 33 for a linear blade passage. The other endwall profile of the passage is always flat in this case. The surface static pressure P_s on the contoured endwall in figure 33 increases near both the pressure side and suction side compared to the P_s at the same locations on the flat endwall. But, the pitchwise pressure gradient, that drives the cross-pitch flow, in the first 40% axial chord decreases for the contoured endwall compared to that for the flat endwall. This clearly affects the cross-pitch flow on the endwall as shown in figure 33. The turning of the streamlines near the leading edge is much lower on the contoured endwall than on the flat endwall. The distance of the saddle point from the leading edge is also smaller for the contoured endwall than for the flat endwall. This indicates that the leading edge horse-shoe vortex is smaller in size above the contoured endwall. Inside the passage, the streamlines are also turning less toward the suction surface and appear to be more parallel to the blade surface on the contoured endwall. This occurs as the strength of the cross-pitch flow near the contoured endwall is decreased. The consequences of the results in figure 33 are weaker passage vortex and lower total pressure loss across the blade passage with the non-axisymmetric contoured endwall. These will be shown next.

Figure 34 shows the streamlines in a pitchwise plane located 9% axial chord down the passage. The blade profile and contoured endwall profile are identified as solid objects in the figure. The structure of the pressure side leg vortex at this location is very clear near the pressure side of the flat endwall case. On the other hand, the streamlines near the pressure side for the contoured endwall case have not completed the full revolution to create a vortex structure. This happens as the pressure side leg vortex is weakened and reduced in size by the contoured endwall. As the pressure side leg vortex is driven from the horse-shoe vortex, this also validates the assertion that the horse-shoe vortex reduces with the contoured endwall. The passage vortex can be identified in figure 34 at the suction side where the total pressure loss coefficients, C_{pt} are very high. The extent of the passage vortex can be considered for C_{pt}>0.40 in this case. Then, clearly the passage vortex size for the contoured endwall passage is about half of that for the flat endwall linear cascade. The magnitudes of C_{pt} also indicate that the passage vortex is much weaker for the contoured endwall as the C_{pt} are lower for the contoured endwall at the passage vortex location than for the flat endwall. As such, the mass-averaged total pressure loss across the passage reduces significantly with the contoured endwall. Several other profiles of the non-axisymmetric contoured endwall have been tested successfully in blade and vane passages[64]. The results are similar to what we have discussed so far. These endwall profiles reduce the total pressure loss across the blade passage by weakening the endwall cross flows and passage vortex.

Endwall Film Injection: Coolant air injected through tiny holes in the endwall covers the endwall with a layer of film of cold air and protects the endwall from the hot gas streak in the blade passage (figure 35). Wall static pressure changes in the vicinity of the coolant injection holes as the coolant jet blocks the boundary

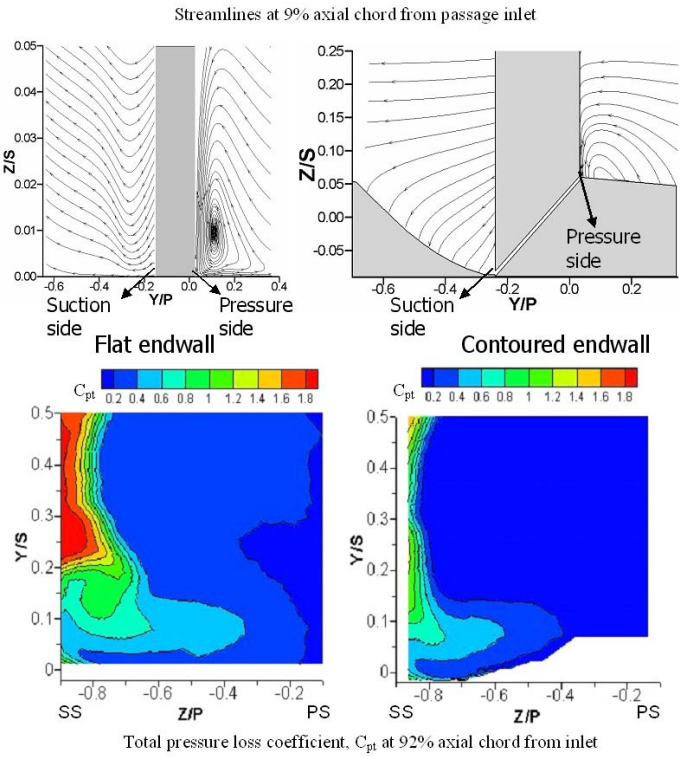

Fig. 34. Streamlines and total pressure loss coefficients with and without non-axisymmetric contoured endwall showing pressure side leg vortex and passage vortex.

Source: See Note 62.

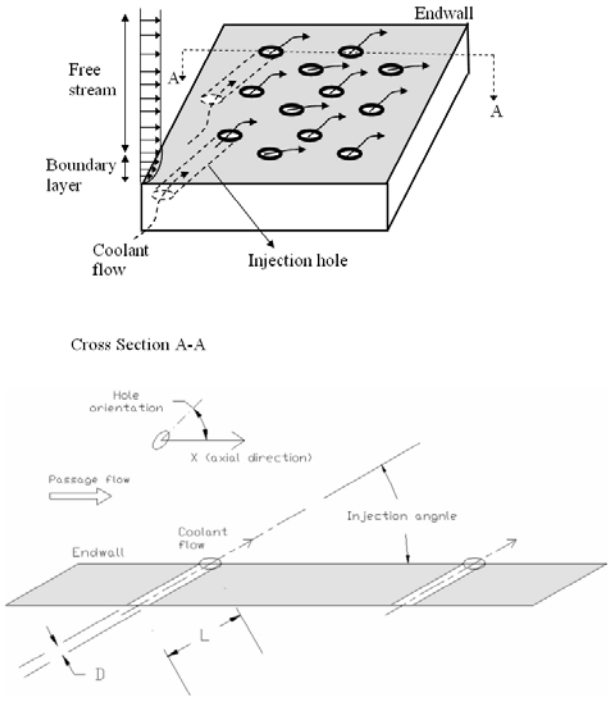

Fig. 35. Coolant injection through holes in endwall for film cooling. L= hole length and D= characteristic scale of hole shape.

layer and interacts with the boundary layer fluid downstream of the hole. Thus, the coolant jets significantly influence the endwall pressure field and the cross-pitch flow in the blade passage. As the coolant jets also interact with the vortex flows, especially with the pressure side leg vortex and suction side leg vortex along the separation line, the secondary flow dynamics changes along with the total pressure losses across the passage. As mentioned in the beginning of Section 4.3-7 that the coolant film is lifted away from the endwall by these vortices, the separation lines in the passage is sometimes termed as the "lift-off" line. The physics of mixing and diffusion of the jets in the boundary layer and interactions between a coolant jet and the boundary layer or the vortices are frequently complicated by the action of neighboring coolant jets. Such physics are studied under the subject of "Jets in Cross Flow" and hence, will not be discussed here. The primary objective of this section is to discuss the effects of the film injection on the secondary flow field and not the dynamics of the jets.

The arrangement of the coolant holes in figure 35 is expected to provide coverage for the entire passage endwall and hence, sometimes is termed as the full-coverage film cooling. The effective coverage of the endwall by the coolant depends on various factors like injection angle, coolant hole orientation, coolant hole shape, hole size, L/D ratio, relative locations of the holes, and mass flux or local blowing ratio from individual hole. These are also the fundamental characteristics of the coolant holes and must all play the role together when the coolant holes are employed. The local blowing ratio is defined as the ratio of the mass flux of the coolant to the mass flux of the passage flow. It is not always easy to measure the mass flux of individual holes with accuracy. Thus, an inlet blowing ratio, M_{inlet} is defined based on coolant flow through an idealized, loss free hole at the passage inlet condition[65].

$$M_{inlet} = \sqrt{\frac{P_{o,plenum} - P_{o,inlet}}{P_{0,inlet} - P_{inlet}}}$$

Here, $P_{o,plenum}$ is the stagnation pressure of the coolant supply plenum, $P_{o,inlet}$ is the stagnation pressure at the passage inlet, and P_{inlet} is the static pressure at the passage inlet. The boundary layer is energized and strengthened with the properly ejected coolant jets. This enables the boundary layer fluid to withstand the pitchwise pressure gradient in the passage and cross-pitch flow is weakened as a consequence. Thus, with proper design and configuration the endwall film injection can also provide an effective structural modification that reduces the secondary flows and aerodynamic losses. It is difficult to generalize the flow field at the endwall when the coolant jets are ejected. Each geometric configuration and flow parameter associated with the coolant holes just mentioned can alter the endwall boundary layer uniquely. On the other hand, the secondary and cross flows affect the coolant jets. The illustrations that are going to be presented next do not represent a typical behavior of the near wall flow. The readers will have some understanding about the relative importance of the coolant jet configuration and secondary flows.

Figure 36 shows the measured locations of the coolant jets as they travel downstream from their ejection points in a linear vane passage[66]. The configuration of the coolant holes is also shown in the figure. The holes are ejecting at 35 degree with respect to the endwall surface. Data are presented near

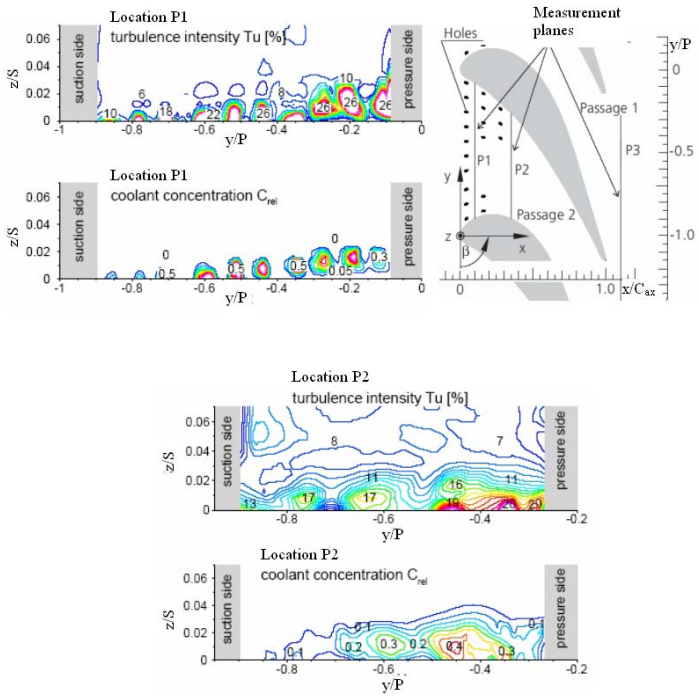

Fig. 36. Coolant jet locations downstream of injection holes in a linear vane passage.

Source: See Note 66.

the endwall where the quantities are affected the most. Location P1 is located along a pitchwise plane just downstream of the first row of holes and location P2 is located along a pitch plane just downstream of the 3rd and last row of holes. The coolant concentration is defined as the ratio of coolant density to the free-stream density[67]. The coolant concentration is the highest at the core of jet. Also, the coolant jets have forced vortex motions at the core[68]. Thus, the locations of the coolant jets in figure 36 can be readily identified at the locations of high turbulence intensity and coolant concentration. At location P1, ten distinct jets with high magnitudes from the ten holes upstream are clearly identifiable. The four jets near the suction side are attached to the endwall while the jets nearest the pressure side appear to be slightly lifted up from the endwall. Local blowing ratio is high near the suction side because the wall static pressure is low there and local blowing ratio is low near the pressure side because the wall static pressure is high there. Thus, the jets have higher momentum near the suction side than the jets near the pressure side. High momentum reduces mixing of the jets with the surrounding flow. Also, the suction side main flow has higher kinetic energy than the pressure side main flow. The high kinetic energy bends the suction side jets toward the endwall and high momentum aids the process. On the other hand, the low momentum jets near the pressure side easily penetrate the low energy main flow and lifts up from the endwall.

At location P2 of figure 36, turbulence intensity Tu>11% near the endwall across the pitch is caused by the combined effects of all coolant jets as Tu is maximum 11% at this location without any coolant injection. Besides the signatures of three jets (Tu≥19%) from the last row of holes near the pressure side, no other jets are distinct at this location. The higher coolant concentration near the pressure side is the result of large number of jets near the pressure side compared to the number of jets near the suction side. In addition, some jets in the first and second rows are directly lifted away from the endwall by the up-wash flows of the pressure side leg vortex and suction side leg vortex. This action mixes the jets easily with the main stream and the coolant concentration from these jets reduces significantly. Some jets on the pressure side may also have been swept toward the middle of the passage by the cross flow and pressure side leg vortex. Thus, the coolant concentration is the highest near y/P=-0.45 at location P2. Similar results about the locations of the coolant jets are reported in a linear vane passage[69].

The effectiveness of individual coolant jet is largely dependent upon its ability to stick persistently to the endwall to provide the maximum coverage. The location chosen for a coolant hole is therefore very important in this respect. Figure 37 provides evidence by how strongly the secondary flows deflect and block some coolant jets simply because of their location[70]. The coolant holes shown in figure 37 are arranged in four pitchwise rows at upstream of leading edge, 30% axial chord, 60% axial chord, and 90% axial chord. Four individual holes are also located at the pressure side of the blade passage. All the holes have same shape and geometry. The dark traces on the endwall are produced by the ejected coolant jets as they travel along the endwall. The length, level of darkness, and lateral spreading of the traces indicate the distance traveled by the jets, level of consistency of coolant, and lateral coverage by the jets, respectively, before they are mixed with the main fluid. Ammonia gas mixed with the coolant air stream reacts with the Diazo coating on the endwall and produces such traces[71]. Surface flow visualization as the coolant jets ejecting indicates the separation or lift-off lines of the pressure side leg/passage vortex and suction side leg vortex in figure 37. The five holes from the pressure side at 30% axial chord and the holes at the last two rows are located downstream of the lift-off line for the pressure side leg vortex. Friedrichs et al. (1996) shows that this line has moved downstream compared to that without coolant injection. The 4th and 5th

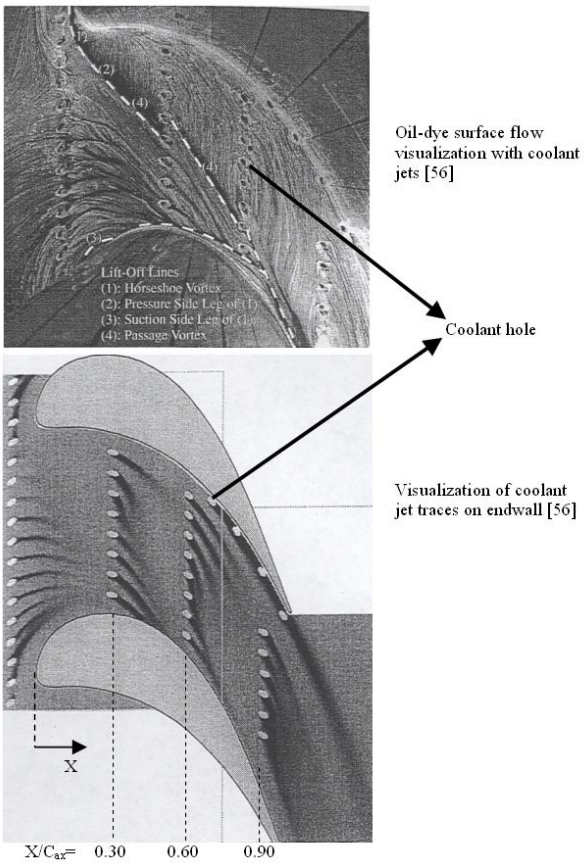

Fig. 37. Visualization of surface flow and coolant jet trajectories along endwall in a linear blade passage at M_{inlet}=1.0.

Source: See Note 70.

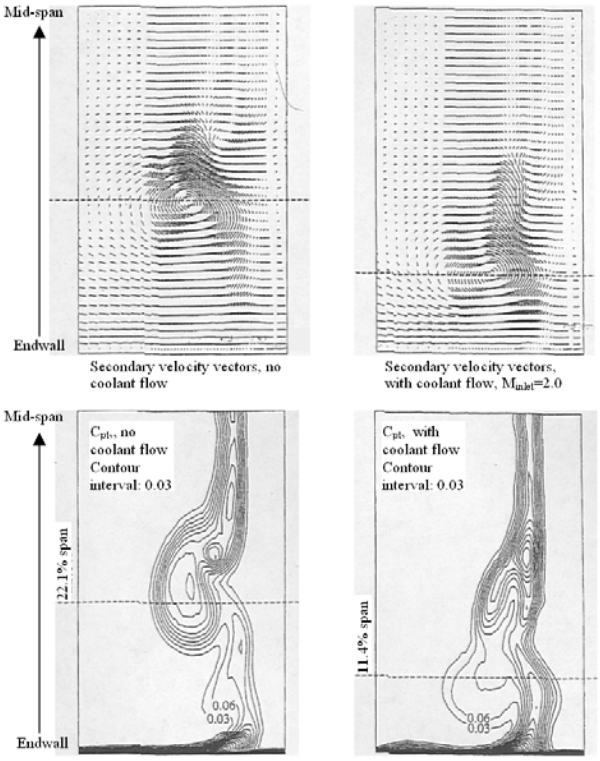

Fig. 38. Passage vortex and total pressure losses at exit flow with (M_{inlet}=2.0) and without coolant injection in a linear blade passage.

Source: See Note 65.

coolant jets from the pressure side at 30% axial chord seem to dislocate the lift-off line slightly downstream from their positions.

The jet traces from the holes located upstream of the passage in figure 37 shows virtually very little or no traces near the pressure side and all jets near the suction side are deflected around the lift-off line. The strong leading edge horse-vortex is either lifting the jets or deflecting the jets even if they are shooting directly toward the leading edge. The jets from the middle holes in the upstream row have low momentum and are aimed toward the pressure side while the cross flow here is directed in the axial direction have low kinetic energy. Thus, these jets have small trajectories and are easily swept in the main flow as soon as they are ejected. The traces of the jets from the holes inside the passage, except those near the pressure side, are swept toward the suction side by the cross flow. Similar behavior of the jets inside a blade passage is also observed[72]. The 3rd to 5th jet from the pressure side at 30% axial chord and 2nd to 4th jet from the suction side at 60% axial chord are additionally pulled in by the passage vortex (see the lift-off line) and in cases, are entrained into the passage vortex at the hole location itself. The traces nearest the pressure side are almost parallel to the pressure side as the boundary layer is very thin here and flow behaves as inviscid. A single jet from one of the four holes at the pressure side corner interacts with and strengthens the jet downstream and the combined jet trajectory is very long at this location. The jets at 90% axial chord and nearest the suction side in the previous two rows eject with high momentum due to the low wall static pressure. The main flow kinetic energy is also high at these locations because of its high speed. These keep these jet traces narrow and stick to the endwall for a longer distance. Also note that the last row of jets are covering a large area on the endwall as they are swept toward the suction side by the cross flow. These jets affect the cross flow as seen in the surface flow visualization of figure 37 (the top image). The streamlines downstream of the holes at 90% axial chord are parallel to the passage rather than being turned toward the suction side as compared to the streamlines upstream of these holes. Thus, these jets have weakened the cross flow near the passage exit.

The effects of the same cooling holes as in figure 37 on the passage vortex structure and total pressure losses at the exit flow are shown in figure 38[73]. But, the inlet blowing ratio for the data with the endwall coolant injection is now 2.0. The plots with no coolant injection are included in figure 38 for comparison. The dashed lines in the figure indicate the spanwise locations of the passage vortex cores. The passage vortex is identified in the vector plot at the location of the clockwise rotation and in the total pressure loss contour at the location of circular region with high loss magnitudes. As noted in both the vector and contour plots, the passage vortex with coolant flow is located much nearer the endwall than with no coolant flow. The momentum of the ejected coolant adds energy to the boundary layer fluid. Therefore, when the passage vortex entrains these boundary layer fluids, the total pressure losses near the bottom part of the passage vortex are reduced. Coolant jets can be injected from continuous slots located in the upstream endwall/platform of the blade passage inlet. This type of coolant flow is often termed as the slot-bleed injection. The readers are referred to note 74 for information on the secondary flow field behavior with the slot-bleed[74].

4.3-9 Notes

1. B. Lakshminarayana, *Fluid Mechanics and Heat Transfer of Turbomachinery* (New York:John Wiley & Sons Inc., 1996).
2. S. L. Dixon, *Fluid Mechanics, Thermodynamics of Turbomachinery*, 3rd ed. (Oxford: Butterworth-Heinemann Ltd., 1995).
3. H. E. Gallus, J. Zeschky, and C. Hah, "Endwall and Unsteady Flow Phenomena in an Axial Turbine Stage," *ASME Tran. J. Turbomachinery 117* (1995): 562-570; E. Boletis, "Effects of Tip Endwall Contouring on the Three-Dimensional Flow Field in an Annular Turbine Nozzle Guide Vane: Part 1- Experimental Investigation," *ASME Tran. J. Engr for Gas Turbines and Power 107* (1985): 983-990; C. H. Sieverding, W. Van-Hove, and E. Boletis, "Experimental Study of the Three-Dimensional Flow Field in an Annular Turbine Nozzle Guidevane," *ASME Tran. J. Engr for Gas Turbines and Power 106* (1984): 437-444.
4. A. Duden, I. Raab, and L. Fottner, "Controlling the Secondary Flow in a Turbine Cascade by Three-Dimensional Airfoil Design and Endwall Contouring," *ASME Tran. J. Turbomachinery 121*(1999): 191-199; S. P. Harasgama and C. D. Burton, "Film Cooling Research on the Endwall of a Turbine Nozzle Guide Vane in a Short Duration Annular Cascade: Part 1- Experimental Technique and Results," *ASME Tran. J. Turbomachinery, Vol. 114* (1992): 734-740.
5. R. P. Dring and W. H. Heiser, *Turbine Aerodynamics*, Chap.4 in Aerothermodynamics of Aircraft Engine Components, AIAA education series (New York: AIAA Inc., 1985).
6. L. Fielding, *Turbine Design- The Effect of an Axial Flow Turbine Performance of Parameter Variation*, (New York: ASME Press, 2000); J.P. Gostelow, *Cascade Aerodynamics*, (OxfordPergamon Press Ltd., Oxford, U.K., 1984).

7. J. L. Kerrebrock, *Aircraft Engines and Gas Turbines*, 2nd ed. (Massachusetts: The MIT Press, 1992).
8. H. Cohen, G. F. C. Rogers, G.F.C., and H.I.H.Saravanamuttoo, *Gas Turbine Theory*, 4th ed. (Essex, U.K.: Longman Group Ltd., 1996); also see note 5 above.
9. H. P. Wang, S. J. Olson, R. J. Goldstein, and E.R.G. Eckert, "Flow Visualization in a Linear Turbine Cascade of High Performance Turbine Blades," *ASME Tran. J. Turbomachinery 119* (1997): 1-8.
10. *Ibid.*
11. *Ibid.*
12 R. Niehuis, P. Lücking, and B. Stubert, "Experimental and Numerical Study on Basic Phenomena of Secondary Flows in Turbines," AGARD Conf. Proc. No. 469, Secondary Flows in Turbomachines (1990): 5.1-5.17. The original version of this material was published by the Advisory Group for Aerospace Research and Development, North Atlantic Treaty Organization (AGARD/NATO) in AGARD Conference Proceedings CP-469 "Secondary Flows in Turbomachines" in 1990.
13. L.S. Langston, "Research on Cascade Secondary and Tip-Leakage Flows- Periodicity and Surface Flow Visualization," *AGARD Conf. Proc. No. 469, Secondary Flows in Turbomachines* (1990): 19.1-19.15; S.H. Moustapha, G.J.Paron, and J.H.T. Wade, "Secondary Flows in Cascades of Highly Loaded Turbine Blades," *ASME Tran. J. Engr. Gas Turbines and Power 107* (1985): 1031-1038. The original version of this material was published by the Advisory Group for Aerospace Research and Development, North Atlantic Treaty Organization (AGARD/NATO) in AGARD Conference Proceedings CP-469 "Secondary Flows in Turbomachines" in 1990.
14. H.P. Hodson and R. G. Dominy, "Three-Dimensional flow in a Low-Pressure Turbine Cascade at Its Design Condition," *ASME Tran. J. Turbomachinery 109* (1987): 177-185.
15. *Ibid.*
16. D.G. Gregory-Smith, C.P. Graves, and J.A. Walsh , "Growth of Secondary Losses and Vorticity in an Axial Turbine Cascade," *ASME Tran. J. Turbomachinery 110* (1988): 1-8.
17. E. Detemple-Laake, "Measurement of the Flow Field in the Blade Passage and Side-wall Region of a Plane Turbine Cascade," *AGARD Conf. Proc. No. 469, Secondary Flows in Turbomachines* (1990): 10.1-10.13. The original version of this material was published by the Advisory Group for Aerospace Research and Development, North Atlantic Treaty Organization (AGARD/NATO) in AGARD Conference Proceedings CP-469 "Secondary Flows in Turbomachines" in 1990.
18. *Ibid.*
19. *Ibid.*
20. W.A. Eckerle and L.S. Langston, "Horseshoe Vortex Formation Around a Cylinder," *ASME Tran. J. Turbomachinery 109* (1987): 278-285.
21. See notes 13 and 20 above.
22. G.I. Mahmood, R. Gustafson, and S. Acharya, "Experimental Investigation of Flow Structure and Nusselt Number in a Low Speed Linear Blade Passage With and Without Leading Edge Fillets," *ASME Tran. J. Heat Transfer 127* (2005): 499-512.
23. See note 20 above.
24. See note 9 above.
25. G.I. Mahmood and S. Acharya, "Experimental Investigation of Secondary Flow Structure in a Blade Passage With and Without Leading Edge Fillets", in review, *ASME Trans. J. Fluids Engineering* (2005);A.K. Saha, G.I. Mahmood, R. Gustafson, and S. Acharya, "Predicted and Measured Flow Field and Heat Transfer in a Linear Blade Cascade Employing Fillets," in preparation for the *ASME Tran. J. Turbomachinery*.
26. See note 9 above.
27. See note 9 above.
28. See note 9 above.
29. See note 9 above.
30. See note 9 above.
31. R. J. Goldstein, H.P. Wang, and M.Y. Jabbari, "The Influence of Secondary Flows Near the Endwall and Boundary Layer Disturbance on Convective Transport From a Turbine Blade," *ASME Tran. J. Turbomachinery 117*(1995): 657-665.
32. See note 25 above.
33. M.B. Kang and K.A. Thole, "Flowfield Measurements in the Endwall region of a Stator Vane," *ASME Tran. J. Turbomachinery 122* (2000): 458-466.
34. See note 14 above.
35. See note 25 above.
36. D. G. Gregory-Smith and J.G.E. Cleak, "Secondary Flow Measurements in a Turbine Cascade With High Inlet Turbulence," *ASME Tran. J. Turbomachinery 114* (1992): 173-183; C. Hah, "A Navier-Stokes Analysis of Three-Dimensional Turbulent Flows Inside Turbine Blade Rows at Design and Off-Design Conditions," *ASME Tran. J. Engr. Gas Turbines and Power 106* (1984): 421-429; L.S. Langston, "Crossflows in a Turbine Cascade Passage," *ASME Tran. J. Engr. for Power 102* (1980): 866-874.

37. K. Hermanson, S. Kern, G. Picker, and S. Parneix, "Predictions of External Heat Transfer For Turbine Vanes and Blades With Secondary Flowfields," ASME Proc. Turbo Expo, GT-2002-30206, 2002.
38. See note 33 above.
39. A. Yamamoto, "Production and Development of Secondary Flows and Losses in Two Types of Straight Turbine Cascades: Part 1- A Stator Case," *ASME Tran. J. Turbomachinery 109* (1987): 186-193;R.P. Roy, K.D. Squires, M. Gerendas, S. Song, W.J. Howe and A. Ansari, "Flow and Heat Transfer at the Hub Endwall of Inlet Vane Passages-Experiments and Simulations," ASME Proc. Turbo Expo, 2000-GT-198, 2000.
40. See note 3 above.
41. See note 3 above.
42. See note 3 above.
43. See note 13 above.
44. See note 13 above.
45. R.G. Dominy and S.C. Harding, "An Investigation of Secondary Flows in Nozzle Guide Vanes," *AGARD Conf. Proc. No. 469, Secondary Flows in Turbomachines* (1990): 7.1-7.15.
46. See note 3 above (Gallus).
47. M.V. Hoyningen-Huene, W. Frank, and A.R. Jung, "Three-Dimensional Time-Resolved Flow Field in the First and Last Turbine Stage of a Heavy Duty Gas Turbine, Part I: Secondary Flow Field," ASME Proc. Turbo Expo, 2000-GT-0438, 2000.
48. J. Zeschky and H.E. Gallus, "Effects of Stator Wakes and Spanwise Nonuniform Inlet Conditions on the Rotor Flow of an Axial Turbine Stage," *ASME Tran. J. Turbomachinery 115* (1993): 128-136.
49. H. Sauer, R. Müller, and K. Vogeler, "Reduction of Secondary Flow Losses in Turbine Cascades by Leading Edge Modifications at the Endwall," *ASME Tran. J. Turbomachinery 123* (2001): 207-213; G. A. Zess and K.A. Thole, "Computational Design and Experimental Evaluation of Using a Leading Edge Fillet on a Gas Turbine Vane," ASME Proc. Turbo Expo, GT-2001-0404, 2001; A.T. Lethander, K.A. Thole, G. Zess, and J. Wagner, "Ortimizing the Vane-Endwall Junction to Reduce Adiabatic Wall Temperatures in a Turbine Vane Passage," ASME Proc. Turbo Expo, GT2003-38939, 2003; S. Becz, M.S. Majewski, and L.S. Langston, "Leading Edge Modification Effects on Turbine Cascade Endwall Loss," ASME Proc. Turbo Expo, GT-2003-38898, 2003;S. Becz, M.S. Majewski, and L.S. Langston, "An Experimental Investigation of Contoured Leading Edges for Secondary Flow Loss Reduction," ASME Proc. Turbo Expo, GT-2004-53964, 2004; also see notes 22 and 25 above.
50. See notes 22 and 25 above.
51. See note 21 above.
52. See note 25 above.
53. See note 49 above.
54. See note 49 above (Zess).
55. S.W. Burd and T.W. Simon, "Flow Measurements in a Nozzle Guide Vane Passage With a Low Aspect Ratio and Endwall Contouring," ASME Proc. Turbo Expo, 2000-GT-0213, 2000; T.I-P Shih, Y.-L Lin, and T.W. Simon, "Control of Secondary Flows in a Turbine Nozzle Guide Vane by Endwall Contouring," ASME Proc. Turbo Expo, 2000-GT-0556, 2000; V. Dossena, A. Perdichizzi, and M. Savini, "The Influence of Endwall Contouring on the Performance of a Turbine Nozzle Guide Vane," *ASME Tran. J. Turbomachinery 121*(1999): 200-208; F.C. Kopper, R. Milano, and M. Vanco, "Experimental Investigation of Endwall Profiling in a Turbine Vane Cascade," *AIAA Journal, AIAA 80-1089R 19*, No. 8 (August 1981).
56. S. Acharya, "Eendwall Cooling With Endwall Contouring and Leading Edge Fillet," Smi-annual Report Submiited to UTSR, South Carolina, Project No. 02-01-SR098, June 2003-December 2003; D.E. Bohn, K. Kusterer, N. Sürken, and F. Kreitmeler, "Influence of Endwall Contouring in Axial Gaps on the Flow Field in a Four-Stage Turbine," ASME Proc. Turbo Expo, 2000-GT-472, 2000; L.P. Timko, "Energy Efficient Engine High Pressure Turbine Component Test Performance Report," Contract Report for NASA, Report No. NASA CR-168289; also see note 55 above (Shih).
57. See note 55 above (Burd).
58. See note 55 above (Dossena).
59. *Ibid.*
60. See note 3 above (Boletis).
61. See note 55 above (Dossena).
62. R. Gustafson, G.I. Mahmood, and S. Acharya, "Control of Secondary Flows in a Low Speed Blade Cascade with a Non-axisymmetric 3-D Endwall," in preparation for the *ASME Trans J. Turbomachinery*.
63. N. W. Harvey, M.G. Rose, M.D. Taylor, S. Shahpar, J. Hartland, and D.G. Gregory-Smith, "Nonaxisymmetric Turbine End Wall Design: Part I- Three-Dimensional Linear Design System," *ASME Tran. J. Turbomachinery 122* (2000): 278-285; J.C. Hartland, D.G. Gregory-Smith, and M.G. Rose, "Non-axisymmetric Endwall Profiling in a Turbine Rotor Blade," ASME Proc. Turbo Expo, 98-GT-525, 1998.
64. G. Ingram, D.G. Gregory-Smith, M. Rose, N. Harvey, and G. Brennan, "The Effect of End-wall Profiling on Secondary Flow and Loss Development in a Turbine Cascade," ASME Proc. Turbo Expo, GT-2002-30339, 2002; J.C. Hartland, D.G. Gregory-Smith, N.W. Harvey, and M.G. Rose, "Nonaxisymmetric Turbine End Wall Design: Part II- Experimental

Validation," *ASME Tran. J. Turbomachinery 122* (2000): 286-293; J. Yan, D.G. Gregory-Smith, and P.J. Walker, "Secondary Flow Reduction in a Nozzle Guide Vane Cascade by Non-axisymmetric End-wall Profiling," ASME Proc. Turbo Expo, 99-GT-339, 1999.

65. S. Friedrichs, H.P. Hodson, and W.N. Dawes, "Aerodynamic Aspects of Endwall Film-Cooling," *ASME Tran. J. Turbomachinery 119* (1997): 786-793.
66. F. Kost, and F. Nicklas, "Film-Cooled Turbine Endwall in a Transonic Flow Field: Part I- Aerodynamic Measurements," ASME Proc. Turbo Expo, 2001-GT-0145, 2001.
67. *Ibid.*
68. F. Bario, F. Leboeuf, A. Onvani, and A. Seddini, "Aerodynamics of Cooling Jets Introduced in the Secondary Flow of a Low-Speed Turbine Cascade," *ASME Tran. J. Turbomachinery 112* (1990): 539-546.
69. *Ibid.*
70. S. Friedrichs, H.P. Hodson, and W.N. Dawes, "Distribution of Film-Cooling Effectiveness on a Turbine Endwall Measured Using the Ammonia and Diazo Technique," *ASME Tran. J. Turbomachinery 118* (1996): 613-621.
71. M.Y. Jabbari, K.C. Marston, E.R.G. Eckert, and R.J. Goldstein, "Film Cooling of the Gas Turbine Endwall by Discrete-Hole Injection," *ASME Tran. J. Turbomachinery .118* (1996):. 278-284; also see note 70 above.
72. *Ibid.*
73. See note 65 above.
74. H.D. Pasinato, Z. Liu, R.P. Roy, W.J. Howe, and K.D. Squires, "Prediction and Measurement of the Flow and Heat Transfer Along the Endwall and Within an Inlet vane Passage," ASME Proc. Turbo Expo, GT-2002-30189, 2002; S.W. Burd and T.W. Simon, "Effects of Slot Bleed Injection Over a Contoured Endwall on Nozzle Guide Vane Cooling Performance: Part I- Flow Field Measurements," ASME Proc. Turbo Expo, 2000-GT-0199, 2000; R. Oke, T.W. Simon, T. Shih, B. Zhu, Y.L. Lin, and M. Chyu, "Measurements Over a Film-Cooled, Contoured Endwall with Various Coolant Injection Rates," ASME Proc. Turbo Expo, 2001-GT-0140, 2001.

BIOGRAPHY

4.3 Turbine Blade Aerodynamics

Sumanta Acharya

Louisiana State University
CEBA 1419B, Mechanical
Engineering Department
Baton Rouge, LA 70803

phone: (225) 578-5809
email: acharya@me.lsu.edu

Sumanta Acharya is currently the L. R. Daniel Professor in Mechanical Engineering, and the Director of the Turbine Innovation and Energy Research (TIER) Center at Louisiana State University (LSU), Baton Rouge . He received his B.S. in Mechanical Engineering from IIT-Kharagpur, India, in 1978, his Ph.D. in Mechanical Engineering from the University of Minnesota in 1982, and has been on the faculty at LSU since 1982. He has worked in several areas pertaining to turbine blade cooling and aerodynamics including internal cooling, film cooling, blade tip leakage flows, and 3D endwall flows (hub). In the gas turbine area he has received funding from Pratt & Whitney, General Electric, the University Turbine Systems Research Program (UTSR) of the Department of Energy, the U. S Navy, the Air Force Office of Scientific Research, the National Science Foundation, and the State of Louisiana. He has published 130 journal articles and book chapters, and presented over 160 conference papers.

Gazi Mahmood

Louisiana State University
CEBA 1419B, Mechanical
Engineering Department
Baton Rouge, LA 70803

Dr. Gazi Mahmood is currently working as a postdoctoral research associate at the Turbine Innovation and Energy Research (TIER) Center of the Louisiana State University. He received his B.Tech. in Mechanical Engineering from the Indian Institute of Technology in Bombay in 1995 and his Ph.D. in Mechanical Engineering from the University of Utah in 2001. The research interests of Dr. Gazi Mahmood include turbulent channel flows, fluid dynamics and convective heat transfer on special surface structures, aerodynamics, gas turbine cooling, pumps, infrared imaging techniques, flow control on wing-shaped bodies, fluidic actuators, and miniature contact probes for flow measurements. Presently, he has been working in a research project investigating the aerodynamic performances and endwall cooling in the gas turbine passages with endwall contouring and leading edge fillets. His work experiences also include research on dimples, pin-fins, and vortex passage employed in heat exchangers, wing bodies, bearing cooling, and turbine blade cooling. He was a lecturer at the Mechanical Engineering Department in Columbia University (New York) in 2001.